Abstract.

This paper examines two internal lee wave closures that have been used together with ocean models to predict the time-averaged global energy conversion rate into lee waves and dissipation rate associated with lee waves and topographic blocking: the *Garner* (2005; "*G05*") scheme and the *Bell* (1975; "*B75*") theory. The closure predictions in two Southern Ocean regions where geostrophic flows dominate over tides are examined and compared to microstructure profiler observations of the turbulent kinetic energy dissipation rate, where the latter are assumed to reflect the dissipation associated with topographic blocking and generated lee wave energy. It is shown that, when applied to these Southern Ocean regions, the two closures differ most in their treatment of topographic blocking. For several reasons, pointwise validation of the closures is not possible using existing observations, but horizontally averaged comparisons between closure predictions and observations are made. When anisotropy of the underlying topography is accounted for, the two horizontally averaged closure predictions near the seafloor are approximately equal. The dissipation associated with topographic blocking is predicted by the *G05* scheme to account for the majority of the depth-integrated dissipation over the bottom 1000 meters of the water column, where the horizontally averaged predictions lie well within the spatial variability of the horizontally averaged observations. Simplifications made by the *G05* scheme that are inappropriate for the oceanic context, together with

Sciences, McGill University, Montreal, CAN

imperfect observational information, can partially account for the prediction-observation disagreement, particularly in the upper water column.

[2]Department of Earth and Environmental

Sciences, University of Michigan, Ann Arbor, USA

[3]Department of Earth, Ocean and Atmospheric Sciences, University of British Columbia, Vancouver, CAN

[4]Climate Change Research Centre and ARC Centre of Excellence for Climate System Science, University of New South Wales, Sydney, AUS

[5]Physical Oceanography Department, Woods Hole Oceanographic Institution, Woods Hole, USA

[6]NOAA/Geophysical Fluid Dynamics Laboratory, Princeton, New Jersey, USA

[7]Ocean and Earth Science, University of Southampton, National Oceanography Centre Southampton, Southampton, UK

[8]Met Office Hadley Centre, Exeter, UK

1. Introduction

The primary objectives of this manuscript are twofold. First, we aim to better understand the parameter sensitivities in two internal lee wave closures that have been employed in numerical models to account for energy conversion into lee waves and to predict energy dissipation rates associated with lee waves and topographic blocking effects. Second, we compare the closure predictions to available observations of dissipation rates. Improving our understanding of lee wave closures is important because topographic blocking effects and internal lee wave generation and dissipation in the vicinity of topography must be parameterized in large-scale ocean models. Here, the term "lee wave closures" can refer to closures that attempt to represent topographic blocking effects as well as lee wave effects. Although topographic blocking effects are not wave-like, strictly speaking, they are lumped into what we refer to as lee wave closures because both topographic blocking and lee waves arise from flow over rough topography.

The relevant horizontal length scales of lee waves range from meters to tens of kilometers and as such are generally smaller than the grid spacing of even state-of-the-art present-day ocean general circulation models. In order to make progress on the task of parameterization, there is a need to better understand both the differences between lee wave closure predictions and local observations of turbulent kinetic energy dissipation rates (*Waterman et al.*, 2013 - see their Fig. 15; *Sheen et al.*, 2013 - see their Fig. 12), as well as the processes that are important in both the generation of lee waves and topographic blocking effects. This manuscript ultimately argues for the need to collect particular observations to test the assumptions made by the two lee wave closures considered here.

Evidence is mounting (e.g., *Naveira-Garabato et al.*, 2004; *Marshall and Naveira-Garabato*, 2008; *Nikurashin and Ferrari*, 2010a,b; *St. Laurent et al.*, 2012; *Waterman et al.*, 2013; *Sheen et al.*, 2013) that energy is lost to internal lee waves when geostrophic flow impinges upon rough topographic features. Internal lee wave formation, radiation, and breaking are thought to contribute substantially to the oceanic momentum, vorticity, and energy budgets [*Naveira-Garabato et al.*, 2013; *Trossman et al.*, 2013, 2015] and to water mass transformation in the Southern Ocean [*Nikurashin and Ferrari*, 2013]. However, considerable uncertainty remains about the global energy conversion rate of geostrophic flow into internal lee waves. Available global estimates range from $0.2 - 0.75$ TW [*Nikurashin and Ferrari*, 2011; *Scott et al.*, 2011; *Wright et al.*, 2014]. Further, a significant mismatch exists between the predictions of local energy conversion and the observed local dissipation in key Southern Ocean regions [*Waterman et al.*, 2013; *Sheen et al.*, 2013]. At present, this mismatch is difficult to attribute to deficiencies in the energy conversion rate prediction versus other causes for discrepancy such as an influence of non-local effects. Given the large uncertainty in these various energy conversion rate estimates, their dependence on the lee wave closures they utilize, and the unlikelihood of directly observing the global energy generation and dissipation rates, it is critical to compare predictions from the lee wave closures with the sparse observations we have.

Here, we focus on existing closure predictions of lee wave energy conversion and dissipation, their representation of topographic blocking, and the uncertainties that arise in the presence of finite-amplitude, two-dimensional topography. Topographic blocking of flow over a one-dimensional representation of topography behaves differently from topographic blocking of flow over a two-dimensional representation of topography and as such is a leading candidate for the cause of differences and uncertainties in the various closure predictions. Hydraulic effects

and low-level breaking occur when a one-dimensional (isotropic) representation of the underlying topography is utilized in closures, as was considered in *Nikurashin and Ferrari* [2011], *Waterman et al.* [2013], *Sheen et al.* [2013], and *Melet et al.* [2014, 2015]. There are additional effects due to vortex shedding, flow separation, and low-level jets when a two-dimensional (anisotropic) representation of the underlying topography is utilized [*Baines*, 1995], as was considered in *Scott et al.* [2011], *Trossman et al.* [2013], *Wright et al.* [2014], and *Trossman et al.* [2015]. The effects of anisotropy can only be included in a two-dimensional power spectrum of topography. One hypothesis for the mismatch between predictions for the local lee wave energy conversion rate and the local observed energy dissipation rate found in *Waterman et al.* [2013] and *Sheen et al.* [2013] is that one-dimensional representations of the topography were used in their calculations. Quantifying the sensitivity of closure predictions to the prescription of the underlying topographic features with particular spectral representations is one key motivator of this work.

There are several lee wave closures that could be implemented as parameterizations in ocean models. While there are closures for internal waves generated by background tidal flows (e.g., *Jayne and St. Laurent*, 2001; *Nycander*, 2005), we focus on the *Bell* (1975; "*B75*" hereafter) and *Garner* (2005; "*G05*" hereafter) closures, applied to background geostrophic flows. The *B75* and *G05* closures have been applied to observations (e.g., *Waterman et al.*, 2013; *Sheen et al.*, 2013) and inserted into model simulations (e.g., *Melet et al.*, 2014; *Trossman et al.*, 2013 and 2015). As in *Melet et al.* [2014], *Trossman et al.* [2013, 2015] found that the stratification in an ocean model is significantly reduced by the introduction of an internal lee wave parameterization. Unless otherwise specified, we will be referring to the energy dissipation rate predictions

from the *G05* scheme and the energy conversion rate predictions from the *B75* theory simply as "closure predictions".

Bretherton [1969] formulated a theory, later extended by *B75*, that relates a two-dimensional representation of the underlying abyssal hill topography, the generating background flow velocity, and the background stratification to the energy conversion rate into lee waves. The *B75* theory was utilized in the *Nikurashin and Ferrari* [2011] and *Scott et al.* [2011] estimates of global energy conversion rate into internal lee waves. Not all energy associated with low-frequency flow impinging upon rough topography is converted into lee waves, as blocking and deflection of the low-level flow also dissipate energy. Thus, the *B75* theory has been modified in some studies (e.g., *Scott et al.*, 2011) to account for partially blocked or partially deflected flow through an empirical Froude number condition that reduces the energy conversion rate into lee waves. *Melet et al.* [2014] parameterized diapycnal mixing due to internal lee waves, based on the lee wave energy conversion rates of *Nikurashin and Ferrari* [2011], and then inserted the diffusivities into an ocean general circulation model.

An alternative lee wave closure is that of *G05* who formulated a scheme for the horizontal momentum sink due to the interaction of a stratified atmosphere with orography. The *G05* scheme has been applied to low-frequency oceanic flows impinging upon bottom topography [*Trossman et al.*, 2013, 2015] as well as to oceanic tidal flows [*Arbic et al.*, 2004, 2010]. The *G05* scheme uses dimensional analysis and an empirical Froude number to account for partially blocked or partially deflected flow, adjusting independently for each topographic feature. *Trossman et al.* [2013, 2015] inserted the *G05* wave drag scheme into the momentum equations of an eddy-resolving global ocean-only simulation, and found that wave drag dissipates about 0.4 TW. Their globally integrated dissipation by wave drag considers the joint effect of the drag

associated with lee waves and topographic blocking. As such, their globally integrated dissipation rate cannot be considered to be an energy conversion rate into lee waves generated by background geostrophic flows, unless the topographic blocking effect is negligible. We elucidate the individual contributions of the lee wave and topographic blocking effects here.

When particular assumptions are made, predictions from the *B75* and *G05* closures can be compared with each other and with observed energy dissipation rates from microstructure profilers. One assumption underlying a local closure versus observed dissipation comparison is that non-local events resulting from mean flow advection and/or lateral wave propagation combined with spatial inhomogeneity in the wave field are small. Every implementation of the *B75* and *G05* closures as parameterizations in prognostic ocean models [*Trossman et al.*, 2013; *Melet et al.*, 2014; *Trossman et al.*, 2015] has assumed that non-local effects are negligible. Because this assumption may break down in some locations, we do not generally expect the local prediction from the *B75* theory or *G05* scheme to equal the local observed energy dissipation rate. However, a comparison of the spatially averaged closure predictions with each other and with observed depth-integrated dissipation rates can provide a useful indication for the importance of particular parameters such as our characterization of the underlying topography. Another assumption is that sampling issues with the profilers, discussed in section 4.4, are of negligible importance to the comparison between closure predictions and the observed depth-integrated energy dissipation rate after a horizontal spatial average is applied. For a preliminary comparison, we first assume that the closures can be evaluated using only profiler data near the seafloor. We then also perform an observational comparison utilizing data throughout the water column.

This manuscript is organized as follows. In section 2, we describe the lee wave closures in more detail. The Southern Ocean observational data used as inputs to the closures and as

points of comparison to the closure predictions are described in section 3. Section 4 begins with an examination of the sensitivities of the closure predictions to features of the underlying topography. We then compare the closure predictions with microstructure observations of the depth-integrated dissipation rate, under the assumption that all momentum flux is deposited near the seafloor. Finally, we assess the sensitivity of the closure predictions to assumptions about the vertical distribution of the lee wave momentum flux before concluding with section 5.

2. Lee wave closures

In this section, we review the two internal lee wave closures considered in this paper, as well as various representations of the underlying topography that each closure requires as input.

2.1. Spectral representation of abyssal hill rough topography

In order to arrive at lee wave closure predictions, we need a representation of the bottom topography. Here, we present multiple spectral representations, including all of the representations that have been used in previous studies. The spectral representation of the underlying topography is a field that represents relevant statistical features of the underlying terrain at each grid point. *Goff and Jordan* [1988] demonstrated the applicability of a two-dimensional representation of the von Kàrmàn statistical model for abyssal hill morphology, the primary component of small-scale seafloor roughness. The von Kàrmàn statistical model is a band limited fractal representation, with a power law form at wavenumbers higher than a corner wavenumber, and flat below it.

In the anisotropic spectral form proposed by *Goff and Jordan* [1988], the spectral representation of abyssal hill roughness, $P_{2D}(k,l)$, is specified by five parameters: root mean square height (H_{rms}); the power law exponent (ν_0, also identified as the Hurst exponent); corner wavenum-

bers in the strike and normal-to-strike direction (k_s and k_n, respectively); and the azimuth of the strike direction (ξ_s). The abyssal hill roughness power spectrum can be written as

$$P_{2D}(k,l) = 4\pi\nu_0 H_{rms}^2 |\mathbf{Q}|^{-1/2} (\Upsilon_*^2(k,l)+1)^{-(\nu_0+1)}. \quad (1)$$

Here,

$$\mathbf{Q} = k_n^2 \hat{\mathbf{e}}_\mathbf{n}\hat{\mathbf{e}}_\mathbf{n}^\mathbf{T} + k_s^2 \hat{\mathbf{e}}_\mathbf{s}\hat{\mathbf{e}}_\mathbf{s}^\mathbf{T}, \quad (2)$$

$\hat{\mathbf{e}}_\mathbf{n}$ and $\hat{\mathbf{e}}_\mathbf{s}$ are orthogonal unit vectors ($\hat{\mathbf{e}}_\mathbf{n}^\mathbf{T}\hat{\mathbf{e}}_\mathbf{s} = \mathbf{0}$) normal to and along the strike directions respectively so that $|\mathbf{Q}|^{-1/2} = (k_n^2 + k_s^2)^{-1/2}$, and

$$\Upsilon_*(k,l) = \sqrt{\left(\frac{|\vec{k}|}{k_s}\right)^2 cos^2(\xi-\xi_s) + \left(\frac{|\vec{k}|}{k_n}\right)^2 sin^2(\xi-\xi_s)}, \quad (3)$$

where $\xi = \text{Tan}^{-1}(k/l)$ is the angle clockwise of true north, or azimuth, of the wavenumber vector $\vec{k}$ =(k,l), which has magnitude $|\vec{k}|$. Equation 1 is dependent upon both the zonal (k) and meridional (l) components of the wavenumber vector. Building upon the work of *Goff and Jordan* [1988], *Goff and Arbic* [2010] estimated abyssal hill statistical parameters globally using empirical relationships derived previously between seafloor spreading rate and direction, while taking into account the smoothing effects of sediment cover. *Goff* [2010] then formulated an alternative representation of global abyssal hill statistics over a larger domain of the ocean based primarily on the small-scale roughness of the gravity field measured by satellite altimeters. Although both can be considered realistic renderings, the latter is considered to be more accurate, particularly in more heavily sedimented regions [*Goff*, 2010], such as the Kerguelen Plateau examined by *Waterman et al.* [2013] and in the present study. However, *Goff* [2010] did not estimate azimuthal orientation. Thus, following *Trossman et al.* [2013, 2015], we will utilize the parameter estimates of *Goff* [2010] for H_{rms}, ν_0, k_s, and k_n, and of *Goff and Arbic*

[2010] for ξ_s, to generate the abyssal hill rough topography spectra from Equation 1 used with both the *B75* and *G05* closures here.

An alternative spectral representation of underlying topography, utilized by *Nikurashin and Ferrari* [2011], *Waterman et al.* [2013], *Sheen et al.* [2013], and *Melet et al.* [2014, 2015], is an isotropic simplification of an approximation to the full power spectrum of *Goff and Jordan* [1988]. For $\vec{\tilde{k}} = (\tilde{k}, \tilde{l})$, the wavenumber vector in the reference frame in which $\tilde{k}$ is along and $\tilde{l}$ is across the geostrophic flow, the approximation to the full power spectrum of *Goff and Jordan* [1988] can be written as

$$P_{2D,approx}(\tilde{k}, \tilde{l}) = \frac{2\pi H_{rms}^2(\mu - 2)}{k_0 l_0} \left(1 + \frac{\tilde{k}^2}{k_0^2} + \frac{\tilde{l}^2}{l_0^2}\right)^{-\mu/2}, \tag{4}$$

where k_0 and l_0 are the roll-off wavenumbers for the model spectrum and $\mu/2$ is the spectral slope for the high wavenumbers over which there is an anisotropic roll off. In order to derive an approximated isotropic spectral form of the abyssal hill roughness, $P_{1D,approx}(\tilde{k})$, *Nikurashin and Ferrari* [2011] assumed that lee waves radiate from topographic scales such that $|\vec{k}| = |\vec{\tilde{k}}|$ is much greater than the characteristic wavenumbers of topographic variation, and that the underlying topography is isotropic (i.e., $k_0 = l_0$). Under these assumptions, the approximated isotropic topographic power spectrum is then given by

$$P_{1D,approx}(\tilde{k}) = \frac{1}{2\pi} \int_{-\infty}^{\infty} d\tilde{l} P_{2D,approx}(\tilde{k}, \tilde{l}) \approx H_{rms}^2 k_0^{\mu-2} (\mu - 2) \tilde{k}^{-(\mu-1)}. \tag{5}$$

Here, $P_{1D,approx}(\tilde{k})$ is specified by three parameters obtained by least-squares fits: the topographic height variance (H_{rms}^2), the characteristic wavenumber of topographic variation (k_0), and μ. *Nikurashin and Ferrari* [2011] estimated H_{rms} by making use of single-beam soundings from ship observations with along-track resolution of at least 2 km in water deeper than 500 meters depth. As in *Waterman et al.* [2013] and *Sheen et al.* [2013], we utilize the H_{rms} estimated

by *Nikurashin and Ferrari* [2011] when we use the approximated isotropic topographic power spectrum. Here, we use Equation 5 to find $P_{1D,approx}(\tilde{k})$, we use Equation 1 to find $P_{2D}(k,l)$, and we weight Equation 1 by $|k|/|\vec{k}|$ and integrate out l to find the isotropic spectrum $P_{1D}(\tilde{k})$, in order to gauge how important the assumptions about the underlying topography made by *Nikurashin and Ferrari* [2011], *Waterman et al.* [2013], *Sheen et al.* [2013], and *Melet et al.* [2014, 2015] are to the lee wave closure predictions. (Alternatively, k can be integrated out in Equation 1 to find $P_{1D}(\tilde{l})$, but that procedure leads to conclusions that are qualitatively similar to those we draw in section 4.2.) The approximation provided by $P_{1D,approx}(\tilde{k})$ will be referred to, hereafter, as "approximated isotropy". Anisotropy in the underlying topography is hypothesized to be significant to the lee wave closure predictions because, for any particular location and time, the flow will take on a preferred direction.

G05 uses three topographic statistics, which relate environmental variables via power laws with parameters: γ, ϵ, and β. γ relates the maximum height of topographic features to their horizontal scale, ϵ determines the number density of features as a function of their maximum height, and β establishes the shape of the vertical cross-section of the topographic features (closer to one for more triangle-shaped features). In this study, we set $\gamma = 0.4$, $\epsilon = 0$, and $\beta = 0.5$, as in *G05*. These values are very close (within the nearest tenth) to the values found in the Southern Ocean by *Trossman et al.* [2013], based on computations from the *Smith and Sandwell* [1997] topographic product added to a synthetic realization of small-scale rough topography manufactured with the *Goff and Jordan* [1988] two-dimensional power spectrum derived from the *Goff* [2010] and *Goff and Arbic* [2010] statistical parameters. The reader is referred to *Trossman et al.* [2013] and *G05* (see his appendix) for additional explanation.

Both the *B75* theory and *G05* scheme utilize the hydrostatic assumption, and neither closure accounts for the finiteness of the water column. However, in contrast to the *B75* theory, the *G05* scheme additionally invokes the non-rotating approximation. The *B75* and *G05* closures are understood to be equivalent in the one- or two-dimensional, hydrostatic ($\omega^2 = (\vec{u} \cdot \vec{k})^2 \ll N^2$, for horizontal wavenumber vector, $\vec{k}$), non-rotating ($f^2 \ll \omega^2$, for Coriolis parameter, f), large Froude number (Fr) limits. Here,

$$Fr = \frac{V}{NZ}, \tag{6}$$

where Z is a characteristic topographic height, V is the magnitude of the near-bottom velocity, and N is the near-bottom buoyancy frequency. Our definition of the Froude number is consistent with the definition used in the atmospheric literature, where it is proportional to the velocity, as opposed to the oceanographic literature (e.g., *Waterman et al.*, 2013; *Sheen et al.*, 2013), which generally utilizes the reciprocal of Equation 6 (i.e., $Fr = NZ/V$).

2.2. The *B75* theory

The *B75* theory relates a spectral representation of the topographic field's abyssal hill roughness, $P_{2D}(k,l)$, to the energy conversion rate into lee waves from the geostrophic flow, $\vec{u}$, impinging upon a topography. The energy conversion rate per unit area into lee waves can be expressed as

$$E_{Bell,2D} = \rho \int \int_{|f| \leq \sqrt{(\vec{u}\cdot\vec{k})^2} \leq N} dk dl P_{2D}(k,l) \frac{\vec{u} \cdot \vec{k}}{|\vec{k}|} \sqrt{N^2 - (\vec{u} \cdot \vec{k})^2} \sqrt{(\vec{u} \cdot \vec{k})^2 - f^2}, \tag{7}$$

where ρ is the average abyssal seawater density. Here, integrals over topographic power spectra used to arrive at energy conversion rates into lee waves are only over the radiating wavenumber range

$$\frac{|f|}{V} < |\vec{k}| < \frac{N}{V}; \tag{8}$$

i.e., the range over which internal waves will not be evanescent.

It is important to note that, when isotropy of the underlying topography is assumed, a one-dimensional power spectrum, $P_{1D}(\tilde{k})$ (different from $P_{1D,approx}(\tilde{k})$) can be used instead of the two-dimensional power spectrum, $P_{2D}(k,l)$, in Equation 7. Using either method of assumed isotropy, the energy conversion rate per unit area into lee waves becomes

$$E_{Bell,1D} = \frac{\rho V}{2\pi} \int_{|f|/V}^{N/V} d\tilde{k} P_{1D*}(\tilde{k}) \sqrt{(N^2 - V^2\tilde{k}^2)(V^2\tilde{k}^2 - f^2)}, \tag{9}$$

where $P_{1D*}(\tilde{k})$ is either $P_{1D,approx}(\tilde{k})$ or $P_{1D}(\tilde{k})$. Equations 9 and 7, respectively, will be utilized in section 4.2 to analyze the differences between predictions for the energy conversion rate assuming isotropic (approximated or not) underlying topography and the energy conversion rate predictions assuming anisotropic underlying topography.

The *B75* theory is a linear theory that does not account for the saturation of the energy conversion rate due to topographic blocking (i.e., flow being forced to go around rather than over a topographic feature) when the Froude number is small (supercritical topography if V and N are constant). *Nikurashin and Ferrari* [2011], *Scott et al.* [2011], *Trossman et al.* [2013], *Waterman et al.* [2013], *Sheen et al.* [2013], *Wright et al.* [2014], and *Melet et al.* [2014] all made use of a multiplicative correction factor, E_{fac}, to the *B75* theory's energy conversion rate (utilizing Equation 7 or 9). This correction factor is meant to extend the *B75* theory to account for topographic blocking. Here, we will use the correction factor in the comparison of the *B75* theory with observed near-bottom energy dissipation rates and in the comparison of the predicted energy conversion rates from the *B75* theory with predictions from the *G05* scheme. To be consistent with each of the aforementioned studies, the correction factor used is

$$E_{fac} = (\frac{Fr}{Fr_c})^2, \tag{10}$$

where Fr_c is a critical Froude number. The correction factor defined by Equation 10 acts to suppress the linear prediction of the energy conversion rate in Equations 7 and 9 when the Froude number is small. Equation 10 is only applied when $\sqrt{2}NH_{rms}/V > Fr_c^{-1}$, where the root-mean-square height of the topography (H_{rms}) is in the radiative wavenumber range (*Waterman et al.*, 2013; *Sheen et al.*, 2013; and references therein). The Fr^2 dependence in Equation 10 may be thought of as an alteration of the effective heights and areas over which lee waves are radiated [*Baines*, 1995]. *Nikurashin et al.* [2014] argued for the use of a smaller Froude number (using our definition of Fr) than the one *Waterman et al.* [2013] and *Sheen et al.* [2013] used ($Fr_c = 0.7$) to compare the predicted energy conversion rates with observed turbulent kinetic energy dissipation rates. Thus, in this study we set $Fr_c = 0.7/\sqrt{2}$. A value of Fr_c ranging from 0.7 to 0.75 has been used in previous studies [*Nikurashin and Ferrari*, 2011; *Scott et al.*, 2011; *Waterman et al.*, 2013; *Sheen et al.*, 2013], motivated by laboratory experiments performed on the case when rotation is not believed to have a large influence on Fr_c [*Aguilar and Sutherland*, 2006], as well as by numerical experiments [*Scinocca and McFarlane*, 2000; *Webster et al.*, 2003; *Eckermann et al.*, 2010]. The factor of $\sqrt{2}$ arises from the approximate normalization factor needed to equate the energy conversion rates using one-dimensional power spectra with those using two-dimensional power spectra [*Nikurashin et al.*, 2014]. In order to make our comparisons consistent, we utilize a single value, $Fr_c = 0.7/\sqrt{2}$, for each topographic power spectrum representation described in section 2.1. This critical Froude number is directly comparable to the one described in section 2.3 for the *G05* scheme.

2.3. The *G05* Scheme

G05 developed a theory for the horizontal momentum stress associated with lee wave generation and topographic blocking. The *G05* scheme is exact, as is the *B75* theory, in the limit

of small-amplitude topography. In addition, the *G05* scheme employs dimensional reasoning to account for non-linear topographic blocking effects. The *G05* scheme estimates the horizontal momentum stress (assumed to be equal to the total drag, $\vec{\tau}$) across the bottom boundary when large-scale flow impinges on topography. If $\vec{u}$ is confined to one layer (e.g., the bottom 500 meters, as assumed in *Trossman et al.*, 2013 and 2015) or if the vertical gradient in the horizontal momentum stress ($d\vec{\tau}_{total}(z)/dz$) is a step function (e.g., non-zero with value $\vec{\tau}$ within a wave drag boundary layer depth and zero elsewhere), then the corresponding energy dissipation rate is $\vec{\tau} \cdot \vec{u}$. If the horizontal momentum stress is distributed over a large portion of the water column, the energy dissipation rate is $\int dz d\vec{\tau}_{total}(z)/dz \cdot \vec{u}(z)$, where the integral is over the entire water column. While the *B75* theory predicts a local energy conversion rate into lee waves, our implementation of the *G05* scheme predicts a horizontally local energy dissipation rate. The *G05* scheme's energy dissipation rate prediction includes energy dissipation associated with flow disturbances as well as energy dissipation associated with internal lee waves. Because the *G05* scheme was developed for atmospheric flows, it does not account for the finite depth of the ocean. Furthermore, as is typical in atmospheric lee wave closures, the *G05* scheme does not account for rotation, wave-wave interactions, or wave-mean flow interactions.

Because the interaction of the near-bottom flow with topography is never entirely linear, the *G05* scheme adjusts the flow's momentum for partially blocked or partially deflected flow based on dimensional analysis. The scaling arguments, which employ dimensional analysis, yield a propagating drag, D_p, associated with lee wave generation and breaking; a non-propagating drag, D_{np}, associated with topographic blocking; and a linear drag limit, D^*. This partition is based on a universal parameter (the critical Froude number) that determines the saturation height of a feature for the given large-scale environment. The non-propagating part represents

flow that is blocked or deflected by the part of the topographic feature that remains when the saturation depth is clipped from it. Internal lee waves are launched from this clipped portion and analyzed with linear theory, ultimately yielding a propagating drag upon breaking. The non-propagating drag due to the remaining portion is estimated using dimensional analysis and assumptions about the vertical cross section (see *G05*; *Trossman et al.*, 2013). It is important to note that the non-propagating drag accounts for horizontal momentum stress associated with topographic blocking or splitting, low level breaking, and vortex shedding, which is represented differently in the *G05* scheme than it is in the extended *B75* theory in Equation 10. The *G05* scheme utilizes H_{ref}, determined by Equation A4, as a topographic height scale, whereas the *B75* theory utilizes H_{rms}, determined by an integral over the topographic power spectrum, as a topographic height scale. These two topographic height scales are not equal and are not perfectly correlated with each other because H_{ref} is a clipped local height, whereas H_{rms} is a statistic that summarizes the topographic roughness.

Our implementation of the *G05* scheme can be summarized as follows (see Appendix A for more details and for definitions of all symbols not defined in the main text). Scaling arguments yield a linear drag given by $a_0 \rho N V H_r^2 / L_r$, which *G05* improved upon by first performing an exact linear analysis to get a linear drag,

$$\vec{\tau}^* = \mathbf{T} \cdot \vec{u}, \tag{11}$$

and then performing a scaling argument to infer the propagating and non-propagating parts of the drag. Here, $\mathbf{T}$ is a topographic information tensor which is a function of assumptions made about the underlying topography (see Appendix A). Modifying the linear theory with scaling

arguments, the *G05* scheme arrives at the drag associated with lee wave breaking,

$$\frac{D_p}{D^*}\mathbf{T}\cdot\vec{u} = \frac{\hat{H}_p}{\hat{H}^*}\mathbf{T}\cdot\vec{u}, \tag{12}$$

which is not necessarily the same as the linear theory's prediction, $\mathbf{T}\cdot\vec{u}$. Each of the H variables used here are Froude numbers averaged over an idealized distribution of individual heights. The remaining drag, $a_1\rho V^2 H_r/(FrL_r)$, is the dissipation associated with topographic blocking. Here, the factor of Fr effectively alters the horizontal length scale, L_r, of the topographic feature (with vertical length scale, H_r) at low Froude numbers so that the flow will not make it over the feature [*Lott and Miller*, 1997]. This non-propagating drag can be expressed as (*G05*)

$$\frac{D_{np}}{D^*}\mathbf{T}\cdot\vec{u} = \frac{a_1\hat{H}_{np}}{a_0(1+\beta)\hat{H}^*}\mathbf{T}\cdot\vec{u}. \tag{13}$$

Here, a_0 and a_1 are coefficients associated with the propagating and non-propagating contributions to the drag. When anisotropy in the underlying topography is assumed, the *Goff* [2010] and *Goff and Arbic* [2010] statistical parameters are used to calculate $\mathbf{T}$ through integration of the *Goff and Jordan* [1988] abyssal hill rough topography power spectra over the relevant range of wavenumbers given by (8). Finally, the energy dissipation rate predicted by the *G05* scheme is given by

$$E_{G05} = \vec{u}\cdot\vec{\tau}, \tag{14}$$

where τ is the sum of the right-hand sides of Equations 12 and 13.

The primary difference between the representation of topographic blocking in the *G05* scheme and in the *B75* theory is that in the *G05* scheme, as in *Lott and Miller* [1997], transitions from a linear theory to a nonlinear theory are made through usage of a non-propagating component of the horizontal momentum stress. When the flow is mostly blocked, this transition in the *G05* scheme modifies the linear prediction for the same topographic height scale through use of a

factor on the order of Fr^{-1} (see the ratio of $\hat{H}^*$ to the first term of $\hat{H}_{np}$ in Eq. A3). As Fr gets larger, the transition from a linear to nonlinear theory is modified due to the tapering of the mountain through use of a factor on the order of Fr^{-2} (see the ratio of $\hat{H}^*$ to the second term of $\hat{H}_{np}$ in Eq. A3). These modifications increase the energy dissipation rate prediction. The saturation correction factor applied in the *B75* theory, on the other hand, uses a factor of Fr^2 (see Eq. 10), as in *Stern and Pierrehumbert* [1988], to reduce the energy conversion rate prediction. The *G05* scheme's modification of the linear theory introduces parameters that appear as exponents in power laws relating features of the underlying topography. The parameters that appear in power laws (see section 2.1) can be estimated using the *Goff* [2010] and *Goff and Arbic* [2010] statistical parameters. An additional empirical parameter, the critical Froude number ($\tilde{H}_{crit}$), has been chosen for the *G05* scheme, just as Fr_c was chosen in Equation 10 for the *B75* theory. The momentum flux predicted by the *G05* scheme can be distributed either in a boundary layer or throughout a larger portion of the water column. In this study, when the momentum flux is not allowed to be distributed throughout a large portion of the water column, we assume the boundary layer has a thickness of 500 meters. *Arbic et al.* [2010], *Trossman et al.* [2013], and *Trossman et al.* [2015] made this choice based on the discussion in *St. Laurent et al.* [2002], which was guided by observations of internal tide dissipation in the Brazil Basin [*St. Laurent et al.*, 2001].

3. Observational Data

We test the sensitivity of the *B75* and *G05* lee wave closure predictions in two Southern Ocean regions where we expect significant lee wave generation and where observations of near-bottom velocities, $\vec{u}$, (with magnitude V) and buoyancy frequencies, N, as well as direct microstructure observations of the turbulent kinetic energy dissipation rates, are available. In these regions, and

in the Southern Ocean more generally, we anticipate interactions between background flows and topography to be dominated by geostrophic flows rather than by tidal flows [*Nikurashin and Ferrari*, 2013].

The Southern Ocean Finestructure (SOFine) project provides observations in the Kerguelen Plateau region (Fig. 1a). This region has both strong near-bottom flows associated with Antarctic Circumpolar Current (ACC) jets and geostrophic eddies, as well as small scale [$\mathcal{O}(1-10\text{km})$] topographic features. As such, we expect elevated internal lee wave generation, topographic blocking, and resulting turbulence [*Waterman et al.*, 2013]. Measurements in the SOFine survey were collected in November and December 2008 and include 59 stations spaced by an average distance of 36 km. Station observations generally include simultaneous lowered acoustic Doppler current profiler (LADCP) measurements of velocity and conductivity-temperature-depth (CTD) measurements of temperature and salinity, covering a near-full range of the water column (down to ~ 10 meters from the seafloor). See *Naveira-Garabato* [2009] for details. Simultaneous vertical microstructure profiler (VMP) measurements of the turbulent kinetic energy dissipation rate were also typically taken. These profiles extend from the surface to an average height of about 40 meters above the seafloor. Owing to the relatively smooth topography in the western portion of the study domain and the relatively rough topography in the eastern portion of the study domain, it is helpful to consider the east and west regions of the SOFine domain as being in different Froude number regimes. See *Waterman et al.* [2013] for further details. There is enough information (i.e., about the underlying topography and near-bottom V and N) to predict energy conversion or dissipation rates using existing lee wave closures (see sections 2.1-2.3) from 17 stations from the western portion (high Fr regime) and 38 stations from the eastern portion (low Fr regime) of the SOFine region.

The Diapycnal and Isopycnal Mixing Experiment in the Southern Ocean (DIMES) project provides observations in the Drake Passage region (Fig. 1b). The T1 transect ($\sim 78^o$ W and between 57^o and 64^o S) was performed between December 2010 and January 2011, while the T4 transect (between 55^o and 58^o W and between 55^o and 59.5^o S) was performed in April 2011 (*Sheen et al.*, 2013 - their Fig. 1b). We use the T1 and T4 transects because these two transects span two distinct regimes of Froude numbers with stations along T1 being characterized by large Froude numbers and stations along T4 being characterized by small Froude numbers. Froude numbers in the DIMES region, ranging from less than 1 to almost 20, span a much larger range of Froude numbers than in the SOFine region. In addition, the degree of anisotropy of the underlying topography found along these transects is greater than in the SOFine region. Microstructure data were collected by VMPs using the same method as in *Waterman et al.* [2013], described above, and finestructure data were collected by a CTD (for temperature, salinity, and depth) and LADCP (for velocities). See *Sheen et al.* [2013] for further details. There is enough information to predict energy conversion or dissipation rates using the lee wave closures (see sections 2.1-2.3) from 3 station locations along the T1 transect and 6 station locations along the T4 transect of the DIMES region. The missing information at other stations generally pertains to the underlying topography.

In order to derive V and N representative of the background flow, where V and N are used as inputs to the closures, we average the observed values of V and N in the vertical over the bottom 500 meters. This choice of length scale is justified by the fact that it represents the average lee wave vertical wavelength predicted by linear theory for the scales of V and N under consideration. Averaging over a lee wave vertical wavelength is expected to return a value representative of the wave-free flow. We note that averaging over a larger range of depths

(e.g., 1000 meters) does not change the qualitative conclusions we reach in sections 4.1-4.3. We note further that it is advantageous to restrict our analysis to one that considers the simplest representation of background V and N (i.e., constant near-bottom values) to control for as many tunable parameters as possible. The potential arrays of vertical profiles available in the data are too numerous and nuanced to derive a meaningful representative sample of a profile that varies in the vertical.

4. Results

We first compare the predictions made by various incarnations of the *B75* theory and *G05* scheme in order to better understand their respective sensitivities to input parameters. We utilize the *B75* theory with an approximated isotropic, isotropic (not approximated), and anisotropic spectral form of the abyssal hill power spectrum; and the *G05* scheme with an approximated isotropic and anisotropic spectral form of the abyssal hill power spectrum. For both the *B75* and *G05* closures, we make use of constant station-independent near-bottom velocities (V_{const}) and buoyancy frequencies (N_{const}), as well as the observed station-dependent near-bottom velocities (V) and buoyancy frequencies (N) averaged over the bottom 500 meters. The values used for our constant near-bottom velocities and buoyancy frequencies (see below) are taken from *Nikurashin et al.* [2014] and are utilized here in order to control for the different treatments of the near-bottom velocities and buoyancy frequencies by the two lee wave closures. In sections 4.1-4.4, we assume that all of the momentum flux is deposited within 500 meters of the seafloor. In section 4.5, we allow the *G05* scheme to deposit momentum over a larger portion of the water column.

To simplify the description of our analyses, we use the following shorthand notation:

• "Obs" - uses the microstructure observations of the turbulent kinetic energy dissipation rate averaged over the bottom 500 meters

• "*B75*" - uses the *B75* theory to predict the energy conversion rate into lee waves; the energy conversion rates are calculated using Equation 7 if anisotropic underlying topography is used and Equation 9 otherwise

• "*G05*" - uses the *G05* scheme to predict the energy dissipation rate, $\vec{\tau} \cdot \vec{u}$, where $\vec{\tau}$ is computed with Equation A1 in sections 4.1-4.4; in section 4.5, the *G05* scheme utilizes the full momentum flux deposition procedure outlined in Appendix A

• "approx iso" - uses approximated isotropic underlying topography with Equation 5

• "iso" - integrates out l in Equation 1 to use isotropic underlying topography

• "aniso" - uses anisotropic underlying topography with Equation 1

• "V N" - uses station-dependent observed velocities and buoyancy frequencies averaged over the bottom 500 meters

• "V_{const} N_{const}" - uses $V = 0.1$ m s^{-1} and $N = 10^{-3}$ s^{-1}, consistent with *Nikurashin et al.* (2014 - their Fig. 7)

• "$Z = H_{ref}$" ("$Z = H_{rms}$") - uses H_{ref} (H_{rms}) for the topographic height scale in the *G05* scheme; H_{ref} is used, by default, in the *G05* scheme, unless otherwise stated with this notation

For example, "*B75* approx iso V N" uses Equation 9 to compute the energy conversion rate estimate of the *B75* theory, Equation 5 for the approximated isotropic topographic power spectrum, and the station-dependent observed velocities and buoyancy frequencies averaged over the bottom 500 meters. To simplify this notation further, we exclude the shorthand notation of the variables whose influence on the closure predictions are not being considered. For example, if the influence of anisotropy is under consideration using the *B75* theory, we only refer to approx

iso, iso, or aniso and drop the reference to the closure and near-bottom velocities and buoyancy frequencies utilized.

In order to quantify the sensitivity of the closure predictions to topographic blocking and to the anisotropy of the underlying topography, the arithmetic average of an energy conversion or dissipation rate and the standard error of that average over all station locations is tabulated as a "reference" (Table 1). A percent difference and a confidence interval for the difference between this reference prediction and another energy conversion or dissipation rate, each arithmetically averaged over all stations, is also given in Table 1. In order to quantify the scatter in each comparison made here, a Pearson correlation coefficient (inversely related to the degree of scatter) and its 95% confidence interval are listed in Table 2. Tables 1 and 2 will be further discussed in sections 4.1-4.4.

To compare the closure predictions to the microstructure observations of dissipation (section 4.4), we first use the observed near-bottom turbulent kinetic energy dissipation rates (Obs). Typically we consider the observed depth-integrated dissipation over a height of 500 meters from the bottom, but we also demonstrate how our comparison of predicted energy conversion/dissipation to observed dissipation would change if we integrated the observed dissipation over a range of depths from the seafloor. In Table 3, we tabulate the depth range over which we would need to integrate the observed dissipation rates in order for the predictions to match most closely to the observed dissipation. It should be noted that these integration depths are approximate. Because the microstructure observations do not sample the full water column to the seafloor, the tabulated heights are too large on account of missing the dissipation in the very near-bottom layer. Table 3 will be further discussed in section 4.4. Lastly, we compare the average vertical profile of the observed dissipation rates with the average vertical profile of the

energy dissipation rates predicted by the *G05* scheme, with allowance made for the lee wave momentum flux to be distributed throughout a large portion of the water column (section 4.5).

4.1. Differences in treatment of topographic blocking

To compare the propagating and non-propagating contributions to the two different closure predictions, and as such the representation of the effects of topographic blocking in each of the two closure schemes, we first control for the complexity of the underlying topography. We use approximated isotropic underlying topography with Equation 5 and only allow H_{rms} to vary from station to station (thus, k_0 and μ are held constant, equal to their station-averaged values). We use $Z = H_{rms}$ for the topographic height scale in each closure with V_{const} N_{const} and set $f = 0$ in the *B75* theory to make it directly comparable to the *G05* scheme. Under these simplifications, allowing $f \neq 0$ does not qualitatively alter the results, which is to be expected because the Coriolis effect is not thought to be important close to the topography in the SOFine and DIMES regions. This is the case because the primary influence of the Coriolis effect on lee wave energy conversion/dissipation is its impact on wave-wave interactions. Here, the vertical scale of the waves is relatively large (N is relatively small), and as such the rate of wave-wave interactions is expected to be small (*Nikurashin and Legg*, 2011). To investigate the subcritical topography (large Fr) limit, we show in Fig. 2a the propagating contribution to the energy dissipation rates from the *G05* scheme versus the energy conversion rates from the *B75* theory, without using the saturation correction factor in the latter. To investigate the supercritical topography (small Fr) limit, we show in Fig. 2b the non-propagating contribution to the energy dissipation rates using the *G05* scheme versus the contribution that the saturation correction factor makes to the *B75* theory's energy conversion rates (i.e., the difference between *B75* without minus with the saturation correction factor). In order to be consistent with *Nikurashin et al.*

(2014 - their Fig. 7), we plot each closure prediction as a function of the inverse of the Froude number, as we define it in Equation 6 here.

Under these simplifications, the two closures offer similar predictions for the propagating contribution to the energy dissipation rate in the subcritical (low inverse Fr) topography limit (Fig. 2a) and for the non-propagating contribution to the energy dissipation rate in the supercritical (high inverse Fr) topography limit (Fig. 2b). However, for moderate subcritical inverse Froude numbers, a discrepancy exists between the two closure predictions. This discrepancy arises from the fact that the two closures account for topographic blocking differently and begin to account for blocking effects at different critical Froude numbers. As a result, at inverse Froude numbers starting at 1, the propagating contribution predictions using the *G05* scheme begin to significantly deviate from the predictions using the *B75* theory that do not account for blocking (Fig. 2a). At inverse Froude numbers larger than 1, the *G05* scheme predicts a non-propagating contribution to the energy dissipation rate that is larger than the corresponding predicted propagating contribution (Fig. 2). At inverse Froude numbers larger than about 0.4, the *B75* theory predicts a larger non-propagating contribution than the corresponding predicted energy conversion rate (Fig. 2). Recall that the modification factor applied in the *G05* scheme to transition a linear theory to a nonlinear one is effectively on the order of Fr^{-2} at smaller inverse Froude numbers and approaches Fr^{-1} at larger inverse Froude numbers (see dashed black lines in Fig. 2b).

4.2. Topographic anisotropy

In this subsection, we investigate the influence of the topographic power spectrum representation on the local and domain-averaged closure predictions. The influence of topographic anisotropy on the predicted energy conversion rate into lee waves is investigated here using the

B75 theory with V_{const} N_{const} and different topographic representations. The saturation correction factor is not included in any of the predictions using the *B75* theory in this subsection so that the confounding effect of topographic blocking is excluded. Our results are qualitatively similar in equivalent computations using the propagating contribution of the *G05* scheme (not shown). We compare *B75* aniso with *B75* approx iso in Fig. 3a and *B75* aniso with *B75* iso in Fig. 3b. We are motivated to compare the influence of approximated isotropic underlying topography with that of anisotropic underlying topography because *Nikurashin and Ferrari* [2011] used the *B75* theory with approximated isotropic underlying topography, while *Scott et al.* [2011] used the *B75* theory with anisotropic underlying topography. *Nikurashin and Ferrari* [2011] and *Scott et al.* [2011] arrived at globally integrated lee wave energy conversion rate estimates more than a factor of two different from each other using different bottom velocity products and different topographic power spectrum representations.

We find that there are considerable pointwise differences in the energy conversion rate predictions depending on whether anisotropic or approximated isotropic topography is assumed (Fig. 3a). At individual station locations, the energy conversion rates from *B75* approx iso and *B75* aniso can differ by up to two orders of magnitude. These two estimates, when spatially averaged over all stations, lie within a factor of two of each other, but this difference remains statistically significant from zero (Table 1). Note that we expect an approximate factor of $\sqrt{2}$ discrepancy between the closure predictions based on the normalization factor needed to equate the energy conversion rates using one-dimensional power spectra with those using two-dimensional power spectra [*Nikurashin et al.*, 2014]. We further note that the topographic representations used by *Nikurashin and Ferrari* [2011] and *Scott et al.* [2011] cannot explain the factor of two difference between their estimates because the *Scott et al.* [2011] estimates

are larger than the *Nikurashin and Ferrari* [2011] estimates, not the other way around. Unless the sign of the difference between the predictions using *B75* approx iso and *B75* aniso reverses when a more globally representative sample is taken, the discrepancy between the *Nikurashin and Ferrari* [2011] and *Scott et al.* [2011] estimates is likely to be explained by their use of different bottom velocity products.

Fig. 3b can be used to ascertain whether pointwise discrepancies in Fig. 3a are due to the isotropic assumption, or to the assumption that $|\vec{k}|$ is much greater than the characteristic wavenumbers of topographic variation (the assumption inherent in the approximation of the isotropy). Because there is little scatter in Fig. 3b (see also the 95% confidence interval on the correlation coefficient in Table 2), the scatter in Fig. 3a is inferred to arise from the assumption that $|\vec{k}|$ is much greater than the characteristic wavenumbers of topographic variation. However, despite the much improved correlation with the anisotropic estimate when the approximation to the isotropy is no longer employed, we see a larger bias in the prediction assuming isotropic as opposed to approximated isotropic topography, with the average discrepancy between the closure predictions using *B75* iso and those using *B75* aniso being larger than that between the closure predictions using *B75* approx iso and those using *B75* aniso (Table 1). It appears that the approximated isotropy assumption can be more accurate than an isotropic topography assumption (at least in a spatial average) because of the multiple parameters (e.g., k_0 and μ) that can be tuned using the approximated isotropy assumption. In general, taking a regional spatial average appears to significantly reduce the discrepancy between the different estimates. While pointwise discrepancies depend upon assumptions made about the underlying topography, the domain-averaged energy conversion rate predictions using an (approximated isotropic or) isotropic representation of the underlying topography are well within an order of magni-

tude of the domain-averaged energy conversion rate predictions using anisotropic underlying topography.

We note that the discrepancies between *B75* aniso and *B75* (approx) iso tend to be larger with larger Froude numbers (Fig. 3). At the station locations where H_{rms} is relatively small, the flows tend to be topographically directed along or across steep slopes (not shown). At these locations, when *B75* aniso is used, the energy conversion rate predictions are relatively large (see large Froude numbers in Fig. 3b). At the same locations, use of the approximated isotropic topography tends to yield artificially large lee wave energy conversion rates (see large Froude numbers in Fig. 3a). These findings combined with the statistically significant differences (Table 1) and correlations (Table 2) between the closure predictions shown in Fig. 3 suggest that the orientation of the underlying topography can play an important role in predicting lee wave energy conversion rates, as the correlation is negative when anisotropic topography is compared with approximate isotropic topography and always significantly positive for all other comparisons.

4.3. Full closure predictions in the bottom 500 meters

Relaxing the simplifications made in previous subsections, we now turn to comparisons of the predictions from the two closures with a station-dependent anisotropic topography as well as station-dependent V and N in place of V_{const} and N_{const}. We also evaluate how the energy dissipation rate predictions from the *G05* scheme compare when different topographic height scales ($Z = H_{rms}$ versus $Z = H_{ref}$) are used. In this subsection, the saturation correction factor is included in all of the predictions using the *B75* theory. In order to demonstrate how the two closures account for topographic effects differently when spatially-dependent (versus constant) velocities and buoyancy frequencies are used, we show scatterplots of the predictions from *G05*

aniso V_{const} N_{const} $Z = H_{ref}$ versus *B75* aniso V_{const} N_{const} (Fig. 4a) and from *G05* aniso V N $Z = H_{ref}$ versus *B75* aniso V N (Fig. 4c). Because the representation of blocking in the *B75* theory sets $Z = H_{rms}$ to evaluate its Fr-dependent correction factor, while the *G05* scheme uses the topographic heights relative to nearby areas ($Z = H_{ref}$), we also analyze how the topographic height scale impacts the energy dissipation rate predictions from the *G05* scheme. To do this, we show predicted energy dissipation rates from *G05* aniso V_{const} N_{const} $Z = H_{rms}$ versus predicted energy conversion rates from *B75* aniso V_{const} N_{const} (Fig. 4b), and also show the predicted energy dissipation rates from *G05* aniso V N $Z = H_{rms}$ versus predicted energy conversion rates from *B75* aniso V N (Fig. 4d).

The topographic height scale utilized by the *G05* scheme impacts the correlation between the closure predictions from the *G05* scheme and *B75* theory. Predictions from *G05* aniso V_{const} N_{const} $Z = H_{rms}$ are almost perfectly correlated with those from *B75* aniso V_{const} N_{const}. In contrast, due to the clipping of the topography such that H_{ref} is at a critical Froude number (see Equation A3), the correlation is much weaker when H_{ref} is used in the *G05* scheme (Table 2; also compare Figs. 4a and 4b). Predictions from *G05* aniso V_{const} N_{const} $Z = H_{rms}$ and *B75* aniso V_{const} N_{const} are almost equivalent (Fig. 4b; Table 1), while the pointwise predictions from *G05* aniso V_{const} N_{const} $Z = H_{ref}$ can be an order of magnitude smaller than the predictions from *B75* aniso V_{const} N_{const} (Fig. 4a). Here again, however, we find that the spatially averaged predictions from *G05* aniso V_{const} N_{const} $Z = H_{ref}$ and *B75* aniso V_{const} N_{const} are less than a factor of two different from each other, and that this difference is not statistically significant from zero (see the 95% confidence interval for their difference, $D_{E,CI}$, in Table 1).

The use of spatially varying near-bottom velocities and buoyancy frequencies also strongly impacts the correlation between the energy conversion rate predictions from the *B75* theory and

the energy dissipation rate predictions from the *G05* scheme. In the case of $Z = H_{rms}$ (the choice of topographic height scale that produces the best correlation between *G05* and *B75* predictions) the use of station-varying V and N reduces the correlation between the predictions from the two closures (Table 2; also compare Figs. 4a,c with Figs. 4b,d). For both the case of $Z = H_{ref}$ and $Z = H_{rms}$, again the scheme predictions can differ by an order of magnitude at individual locations (with the dissipation rates predicted by *G05* being both an order of magnitude larger and smaller than the energy conversion rates predicted by *B75*, depending on location; Fig. 4). However, these discrepancies largely cancel out in the regional average, where they differ by less than a (statistically indistinguishable) factor of two (see $D_{E,CI}$ in Table 1). This is consistent with the findings of *Trossman et al.* [2013], who similarly document order-of-magnitude discrepancies between predictions from *G05* aniso V N $Z = H_{ref}$ and *B75* aniso V N at individual locations, but near-equal global averages. Differences in the treatment of topographic blocking (Fig. 2) and anisotropy in the underlying topography (Fig. 3), the prescription of the topographic height scale, and the dependence on the near-bottom velocity and buoyancy frequency are all partially responsible for the discrepancies between the closure predictions.

4.4. Comparison of closure predictions with observations

We next compare the closure predictions to the microstructure observations of the turbulent kinetic energy dissipation rate. Our goal is to assess how improved representations of the underlying topography impact the comparison of the local predicted energy conversion to the local observed dissipation. Given our finding that better characterization of the underlying topography will significantly alter the closure predictions (section 4.2), it is possible that the use of an approximated isotropic topography assumption with a relatively large Fr_c by *Waterman et al.* [2013] and *Sheen et al.* [2013] is a leading cause of the relatively large discrepancy they

report between observations and the *B75* closure predictions (specifically, they report order of magnitude differences between the energy dissipation rate from observations integrated over the bottom 1000 meters versus the predicted energy conversion rate from *B75* approx iso). Because *Nikurashin et al.* [2014] found that the energy conversion rate predictions from *B75* approx iso were much reduced when they used a smaller value of Fr_c than that used in the *Waterman et al.* [2013] and *Sheen et al.* [2013] calculations, we use $Fr_c = 0.7/\sqrt{2}$, consistent with the advice of *Nikurashin et al.* [2014]. Comparisons of various closure predictions using the observed station-dependent V and N and the observed dissipation rates are given in Tables 1 and 2. Table 3 lists the heights to which the average vertical profiles of observed dissipation rates need to be integrated from the bottom in order to best match each of the closure predictions.

The spatially averaged closure predictions vary widely depending upon how the features of the underlying topography are specified (Table 1). Use of *G05* aniso $Z = H_{rms}$ generates very large mismatches, whereas use of *G05* aniso $Z = H_{ref}$ produces a much closer match with Obs. Use of *B75* approx iso and *B75* iso generate very large mismatches, whereas use of *B75* aniso produces a much closer match with Obs. The two closure predictions closest to Obs (Table 1) utilize anisotropic topography and agree best with observations when the observations are integrated to depths between 500 and 1000 meters above the seafloor (Table 3). These two closure predictions, *G05* aniso $Z = H_{ref}$ and *B75* aniso, are statistically indistinguishable from the observations when the observations are integrated to 500 meters above the seafloor (Table 1). While the spatially averaged predictions using *B75* aniso and *G05* aniso $Z = H_{ref}$ are within 20% of Obs (Table 1), the pointwise discrepancies between these closure predictions and observations can be much larger (not shown). Further, the correlation between these predictions

and the observations is poor and not statistically distinguishable from 0 at a 95% confidence level (Table 2).

There are many observational sampling issues that could contribute to the large pointwise discrepancies between the closure predictions and observed dissipation rates. For example, our assumption that the pointwise measurements of V are representative of the large-scale, low-frequency flow that is relevant for lee wave generation may be a poor one. Another source of potential bias, proposed by *Polzin et al.* [2014], is associated with free-falling microstructure profilers that operate without altimeters (such as the ones utilized in the present study). The deviation in the position of a free-falling profiler from its expected trajectory (e.g., due to downstream advection) can lead to large differences between the deepest depth sampled and the seafloor. This can be particularly problematic on the downslope side of topographic saddles, as the drop weight pressures for the profilers are never set to be deeper than the local bottom, and in this case, downstream advection would cause the deepest depth sampled to be significantly off the seafloor. This has an important effect on attempts to validate topographic blocking in the closures, as we expect elevated non-propagating form drag in these locations owing to the effects of flow separation and vortex shedding.

Inadequacies in the power spectra representation of the underlying topography also may contribute to the pointwise discrepancies. It is possible that our use of the *Goff* [2010] and *Goff and Arbic* [2010] statistical parameters, as opposed to the direct analysis of local multi-beam data, to arrive at the abyssal hill topography power spectra explains a large degree of the scatter found in our closure prediction-observation comparisons. Unfortunately, we do not have sufficient data from multi-beam observations to test this hypothesis.

A few other potential hypotheses for the discrepancies between the lee wave closure predictions and the microstructure observations have already been broached. One is that non-local effects such as wave propagation and/or mean flow advection and spatial heterogeneity in the generated wave field can be important. The findings of *Waterhouse et al.* [2014] could not rule out the hypothesis that these non-local effects explain the deviation from unity that they found in the ratio of local internal wave generation to local dissipation. With existing data, we, like *Waterhouse et al.* [2014] and *Waterman et al.* [2014], are unable to distinguish between the dissipation of locally generated energy versus remotely generated energy that has propagated, advected, and/or reflected from the surface and/or seafloor. Energy exchange between triad members of wave-wave interactions and between waves and the mean flow can also arrest the breaking of internal lee waves [*McComas and Bretherton*, 1977; *Sun and Kunze*, 1999a, b], and this too would lead to a local mismatch between lee wave energy locally generated and energy locally dissipated. Additionally, the prediction-observation mismatch may, in part, be due to the relatively crude assumptions we have made thus far regarding the vertical deposition of momentum. In this latter scenario, a large discrepancy would be expected between the closure predictions and observations at larger Froude numbers because low-level breaking is less likely in such a regime. We consider the impact of the prescription of the vertical distribution of the lee wave momentum flux on the energy dissipation rate predictions in the next section.

It is also possible, of course, that there are inadequacies in the formulation of the closures themselves. For instance, the closures may have an inaccurate treatment of topographic blocking. Potential sampling issues with the profilers, such as the lack of observations very close to the seafloor and the uncertainty about the exact location (height above bottom) of the profilers, inhibit our ability to assess the accuracy of the treatment of topographic blocking in the clo-

sures. The *G05* scheme also expects grid cell-averaged low-pass filtered fields as inputs, such as those given by a general circulation model, rather than the local *in situ* measurements that are utilized here.

4.5. Momentum flux vertical deposition sensitivity

The predictions from the *G05* scheme are in reasonably good agreement with the observations when it is assumed that the horizontal momentum stress is deposited uniformly in the bottom 500 meters and that the relevant observed dissipation is confined to this same near-bottom layer. However, in the actual ocean, the momentum flux and energy dissipation are distributed in the vertical in a more complicated manner. Therefore, we investigate whether the vertical profile of energy dissipation rates predicted by the *G05* scheme, averaged in the horizontal spatial direction, are in closer agreement with the averaged vertical profile of observed dissipation when vertical deposition of lee wave momentum flux over a larger portion of the water column is allowed. At each station location, the predicted profiles using the *G05* scheme are calculated at the finestructure depth levels, sorted into heights above the deepest finestructure measurement, and smoothed with a 500 meter depth running average. Also at each station location, the observational profiles are sampled at the microstructure depth levels, sorted into heights above the deepest microstructure measurement (referred to as the "bottom" hereafter), and smoothed with a 500 meter depth running average. The predictions and observations are then geometrically averaged over DIMES and SOFine station locations and shown in Fig. 5. The deepest measurement for the observed dissipation is from the microstructure profiler data and the deepest measurement for the *G05* scheme predictions is from the finestructure profiler data. These depths are typically within 100 meters of each other. Averaging over all DIMES and SOFine station locations, the deepest microstructure measurement is less than 20 meters different from

the deepest finestructure measurement. A geometric average is used for the profiles because of the relatively small sample sizes at larger heights above the bottom. The deep mixed layer is ignored due to our inability to resolve it with profiler observations and the fact that the vertical extent of the deep mixed layer is generally less than the root-mean square topographic variability. The error statistics in Fig. 5 are computed as the standard deviation over all station locations at each height above bottom of the observed dissipation rate on a base-10 logarithmic scale.

There are qualitative regional differences in the discrepancies between the average predicted dissipation profile and the average observed dissipation profile. The discrepancy between the average predicted dissipation profile and the average observed dissipation profile is more pronounced in the western portions of the DIMES and SOFine regions than in the eastern portions of the DIMES and SOFine regions (Figs. 5a-b). The locations where the discrepancy between the predictions and observations exceeds one spatial standard deviation are above about 1000 meters from the bottom in the western portions of the DIMES and SOFine regions (Fig. 5a) and above about 2750 meters from the bottom in the eastern portions of the DIMES and SOFine regions (Fig. 5b). The average energy dissipation rate prediction from the *G05* scheme, depth-integrated over the bottom 4500 meters, is about 1×10^{-2} (4×10^{-2}) W m^{-2} in the eastern (western) portions of the DIMES and SOFine regions. In comparison to these *G05* predictions, the average observed energy dissipation rate, depth-integrated over the bottom 4500 meters, is about 4×10^{-3} W (3×10^{-3}) W m^{-2} in the eastern (western) portions of the DIMES and SOFine regions. Because the velocities are larger closer to the surface, the amount of predicted dissipation is larger closer to the surface in both the eastern and western portions of the DIMES and SOFine regions.

Considering only the bottom 2000 meters, where we would expect the effects of lee waves and topographic blocking to dominate over other factors, the average predicted dissipation profile over all of the DIMES and SOFine station locations is in reasonably close agreement with the average observed dissipation profile (Figs. 5c). The average predicted dissipation profile is within one spatial standard deviation of the average observed dissipation profile in the bottom 2000 meters. The average predicted dissipation profile is in much closer agreement with the average observed dissipation profile in the bottom 1000 meters than it is in any other depth range.

When depth-integrated over the bottom few thousand meters or less, the average predicted non-propagating contribution to the energy dissipation rate is larger than the average predicted propagating contribution to the energy dissipation rate (Fig. 5d). Due to the different dependencies of the non-propagating and propagating base fluxes upon the environmental variables, $D_{np}/D_p \approx 1000$ (see Eq. A2) when averaged over all station locations. However, when the momentum fluxes associated with the non-propagating and propagating contributions are distributed over a large portion of the water column, the non-propagating contribution is only non-zero up to several hundred meters above the bottom, whereas the propagating contribution is non-zero up to several thousand meters above the bottom. When a depth integral is taken over the portion of the water column where the predictions agree most closely with observations (i.e., the bottom $1000 - 2000$ meters), the non-propagating contribution is still significant because it tends to be an order of magnitude larger than the propagating contribution where both are non-zero. The non-propagating contribution accounts for about 60% (40%) of the energy dissipation in the bottom 1000 (2000) meters. This strongly suggests that the enhancement in observed dissipation near the bottom is primarily due to topographic blocking.

We cannot fully explain the discrepancy between the closures and observations by allowing for the vertical deposition of momentum flux. There are a number of other confounding factors. Observations over the entire deep mixed layer are not available. Also, because the largest source of discrepancy between the average predicted dissipation profiles and the average observed dissipation profiles in the bottom 1000 meters of both the eastern and western portions of the DIMES and SOFine regions is the bottom enhancement of the dissipation, either H_{ref} is not the most appropriate vertical height scale or that our imperfect knowledge of H_{ref} is a significant hinderance to closure validation. This prevents us from being able to assess the adequacy of the scheme's representation of topographic blocking (and, therefore, its prediction of most of the energy dissipation). Further, the formulation of the vertical deposition of momentum flux may be suspect. Three factors not accounted for by the *G05* scheme would act to reduce the energy dissipation rate predictions away from the seafloor (e.g., above about 1000 meters above the bottom in Fig. 5a and above about 2750 meters above the bottom in Fig. 5b). The inclusion of a finite water column (which forces a more accurate level of vanishing drag), the Coriolis effect (which reduces the integration range over which internal waves are not evanescent [see Equation 8]), and wave-wave and wave-mean flow interactions (which trade energy instead of dissipating it) would each reduce the energy dissipation rate predictions. The failure of the *G05* scheme to account for the finiteness of the water column deserves special mention here in the ocean context as it is important that none of the closure predicted momentum flux exits the model domain. We emphasize the findings of *Shaw and Shepherd* [2007] and *Shaw et al.* [2009], which suggest that non-conservation of momentum (e.g., allowance of the momentum flux to exit the ocean surface in ocean only simulations) can have significant implications on the temperature and possibly other fields. At the same time, in a finite water column, momentum may not be strictly

conserved [*Polzin*, 2010], as it can be traded for potential vorticity [*Bühler and McIntyre*, 2005], and have extended dynamical consequences for the interactions of internal waves with eddies [*Polzin*, 2008, 2010; *Arbic et al.*, 2013]. The full vertically deposited momentum flux profiles as implemented here using the *G05* scheme should not be utilized in ocean simulations without carefully addressing these issues.

5. Conclusions and Discussion

This paper examines the sensitivity of the *B75* theory predictions of lee wave energy conversion rates and *G05* scheme predictions of dissipation rates associated with lee waves and topographic blocking to various environmental factors (i.e., topographic anisotropy, specification of the topographic height scale, and the generating flow's velocity and stratification). This paper also compares the spatial averages of closure predictions and observations of the turbulent kinetic energy dissipation rate, and addresses whether the accuracy of the closures can be adequately assessed through this comparison in two Southern Ocean regions. In agreement with *Trossman et al.* [2013], the present study finds that the predictions from the *B75* theory and *G05* scheme for the energy conversion rate and near-bottom energy dissipation rate can differ by up to an order of magnitude at individual locations. However, when averaged in the horizontal spatial direction over the Southern Ocean regions, the predictions from both closures agree to within a factor of two, assuming that anisotropic topography is properly accounted for. The differing treatments of partial topographic blocking at intermediate Froude numbers can explain a significant fraction of the difference between the predictions from the *G05* scheme and *B75* theory.

The predictions from the *G05* scheme, when geometrically averaged in the horizontal spatial direction and distributed throughout a large portion of the water column, lie well within the

spatial variability of the observed energy dissipation within about 1000 meters above the depth of the deepest observational measurement. Due to its large contribution to the dissipation in the bottom 1000 meters, topographic blocking is inferred to be the primary mechanism causing enhanced dissipation near the seafloor. However, there are large differences between the predictions and observations in some locations higher up in the water column. Accounting for wave-wave and wave-mean flow interactions, the Coriolis effect, and the finiteness of the water column in the lee wave closure may act to reduce the discrepancy between the average closure prediction and average observed dissipation higher up in the water column. However, breaking waves from other sources (e.g., wind-driven effects) also impact the energy dissipation near the surface and may be responsible for some of this upper-ocean discrepancy.

In this paper, we did not focus on pointwise comparisons between the closure predictions and the observed energy dissipation rates because the comparisons display significant scatter, likely due to several environmental factors. For instance, any high-frequency intermittency of the near-bottom velocities makes it problematic to correctly estimate the velocity of the low-frequency generating flow from a single-point measurement. Further, it is possible that pointwise discrepancies can be partially explained by our use of statistical parameters to arrive at the abyssal hill topography power spectra instead of the actual topographic power spectra (which are sparsely available). It is also possible that pointwise discrepancies arise due to incomplete sampling of the water column and bias in the free-falling profiler positions due to downstream advection. Lastly, non-local processes, such as advection of the waves by mean flows and the three-dimensional propagation of waves between their generation and breaking sites, may explain part of the pointwise disagreement between the closure predictions and the observed turbulent kinetic energy dissipation rates.

Topographic blocking and energy conversion and dissipation rates associated with lee wave generation must ultimately be accounted for in ocean models. However, the manner in which these effects should be represented in models remains unclear because we are not able to validate some aspects of the lee wave closures using existing observations. When topographic anisotropy is taken into account, the differences between the closure predictions and the observed turbulent kinetic energy dissipation rates are not statistically distinguishable from zero in a spatial average. If this agreement we find between the closure predictions and the observed energy dissipation rates is an indication that non-local effects cancel out when spatial averaging is applied over domains the size of an ocean model grid cell (typically smaller than the DIMES (SOFine) region that can be bounded by a $1000 \times 1271\text{km}^2 = 1,271,000\text{km}^2$ ($785 \times 500\text{km}^2 = 392,500\text{km}^2$) box), then there would be no need to parameterize non-local effects in ocean models. However, several other factors must also be negligible in order for us to conclude that we can validate the lee wave closures in the bottom $500 - 1000$ meters in a spatial average using existing observations. These factors include the possibly inadequate representation of the underlying topography, the variability in the generating flow and dissipation rates on spatial scales of the order of the possible bias in free-falling microstructure profiler positions, asynchronicity of the finestructure and microstructure profiler measurements, and inadequate sampling of the energy dissipation very close to the bottom by the profilers.

Several new observations would be needed to fully validate the lee wave closures. Observations closer to the seafloor are needed everywhere. Observations closer to the bottom, on the downslope side of topographic saddles, are especially needed to validate the non-propagating drag closure predictions. Simultaneous measurements on the downslope side of a topographic feature and downstream between that topographic feature and another are required to assess the

magnitude of non-local lee wave dissipation at individual horizontal locations. For an adequate description of the local topography, either measurements of the full two-dimensional topography, or a new method to calculate a two-dimensional power spectrum of the topography from the limited multi-beam observations that are available at profiler station locations, would be required. Considerable uncertainty remains about the various height scales over which dissipation associated with the propagating and non-propagating components of the predicted drag occurs. We leave for future investigation the questions of whether our conclusions apply to regions outside of the SOFine and DIMES domains, and of whether particular lee wave momentum flux schemes are more appropriate, under particular regimes, than others.

Acknowledgments. The authors would like to thank Michael Messina for his computer support and the two anonymous reviewers for their helpful comments. D. S. Trossman and B. K. Arbic gratefully acknowledge support from National Science Foundation (NSF) grant OCE-0960820 and Office of Naval Research (ONR) grant N00014-11-1-0487. S. Waterman gratefully acknowledges support from the Australian Research Council (Grants DE120102927 and CE110001028) and the National Science and Engineering Research Council of Canada (Grant 22R23085). The SOFine and DIMES data analyzed in this paper can be obtained through the British Oceanographic Data Centre (BODC) by navigating the following links, respectively: http://archive.noc.ac.uk/SOFINE/ and http://dimes.ucsd.edu/en/data/.

Appendix A: Details of the *G05* scheme

G05 developed a linear theory, described in detail below, for the horizontal momentum stress associated with lee wave generation and breaking. The *G05* scheme determines the direction and magnitude of the near-bottom horizontal momentum stress, via linear theory, from the spectrum

of the topography and from the direction and magnitude of the impinging flow. Therefore, in order to define each of the components of the horizontal momentum stress, a characterization of the relation between the horizontal momentum stress and the statistical properties of the bottom topography is required. We are interested in the small scale roughness of the topography within the range of relevant wavenumbers specified by (8). We work with the abyssal hill rough topography power spectrum of *Goff and Jordan* [1988], $P_{2D}(x, y; k, l)$, using the parameters from *Goff* [2010] and *Goff and Arbic* [2010], and integrate over all relevant wavenumbers given by (8) to calculate the topographic information tensor [*Trossman et al.*, 2013, 2015],

$$\mathbf{T} = \frac{\rho N}{(2\pi)^2} \begin{pmatrix} \int dk \int dl P_{2D}(k,l) \frac{k^2}{|\vec{k}|} & \int dk \int dl P_{2D}(k,l) \frac{kl}{|\vec{k}|} \\ \int dk \int dl P_{2D}(k,l) \frac{kl}{|\vec{k}|} & \int dk \int dl P_{2D}(k,l) \frac{l^2}{|\vec{k}|} \end{pmatrix}.$$

(When a one-dimensional topographic power spectrum is used, the topographic information tensor becomes one-dimensional, $T = (\rho N)/(2\pi) \int d\tilde{k} \tilde{k} P_{1D*}(\tilde{k})$, and the notation used here is defined in sections 2.1-2.2.) We use $\mathbf{T}$ (units [kg m^{-2} s^{-1}]), the information tensor, together with the near-bottom velocities, $\vec{u}$, and buoyancy frequencies, N. We compute the horizontal momentum stress via

$$\vec{\tau} = (\tau_x, \tau_y) = \left(\frac{D_p}{D^*} + \frac{D_{np}}{D^*} \right) (\mathbf{T}\vec{u}), \tag{A1}$$

where the linear limit (D^*), propagating component (D_p), and non-propagating component (D_{np}) of the horizontal momentum stress are obtained by integrating the drag over an assumed distribution of individual mountain heights in the range (H_{min},H_{max}). (This distribution is defined by the individual mountain heights, not a continuous distribution, derived from the *Smith and Sandwell* [1997] dataset.) This yields

$$D^* = a_0 D_0 \hat{H}^*, \tag{A2}$$

$$D_p = a_0 D_0 \hat{H}_p,$$

$$D_{np} = a_1 D_0 \frac{\hat{H}_{np}}{1+\beta},$$

where

$$D_0 = \frac{\rho V^3 H_r^\gamma}{N L_r} \frac{2\gamma - \epsilon}{H_{max}^{2\gamma-\epsilon} - H_{min}^{2\gamma-\epsilon}}, \tag{A3}$$

$$\hat{H}^* = \left(\frac{H_{max}^{2+\gamma-\epsilon} - H_{min}^{2+\gamma-\epsilon}}{2+\gamma-\epsilon} \right),$$

$$\hat{H}_p = \left(\frac{H_{clip}^{2+\gamma-\epsilon} - H_{min}^{2+\gamma-\epsilon}}{2+\gamma-\epsilon} + H_{crit}^{2+\beta} \frac{H_{max}^{\gamma-\epsilon-\beta} - H_{clip}^{\gamma-\epsilon-\beta}}{\gamma-\epsilon-\beta} \right),$$

$$\hat{H}_{np} = \left(\frac{H_{max}^{1+\gamma-\epsilon} - H_{clip}^{1+\gamma-\epsilon}}{1+\gamma-\epsilon} - H_{crit}^{1+\beta} \frac{H_{max}^{\gamma-\epsilon-\beta} - H_{clip}^{\gamma-\epsilon-\beta}}{\gamma-\epsilon-\beta} \right).$$

Here, L_r is an arbitrary length scale and H_r is an arbitrary height scale. The minimum and maximum terrain heights, $H_{min} = 0.1 H_{max}$ and $H_{max} = \sqrt{\gamma/(2-\gamma)} H_{ref}$, are computed in the manner suggested by *G05* and normalized by V/N, the internal scale. The topographic relief is given by

$$H_{ref}(\vec{x}) = h(\vec{x}) - min\{h(\vec{x})\}, \tag{A4}$$

where $min\{h(\vec{x})\}$ is the minimum seafloor depth amongst the stations in the observational SOFine or DIMES dataset (section 3). (The seafloor depth is approximated by the deepest depth at which observations were taken. Using this approximation, H_{ref} is unbiased as long as the deepest depth at which observations were taken is consistently the same distance above the seafloor. This is about 40 meters in the SOFine data, as stated earlier.) The aforementioned clipping (see section 2.3) is accomplished by evaluating $H_{clip} = min\{H_{max}, max\{H_{min}, H_{crit}\}\}$ and $\tilde{H}_{crit} = N H_{crit}/V$ is the critical nondimensional height that determines the degree to which the flow is blocked. The critical nondimensional height is a constant parameter in this scheme, leaving H_{crit} to be flow-dependent. We set $\tilde{H}_{crit} = 0.7$. The coefficients for the propagating and non-propagating components of horizontal momentum sink ($a_0 = 1$ and $a_1 = 6.3$, respectively)

are set as in *Arbic et al.* [2004] and *Trossman et al.* [2013]. These choices were made based on power law relations between topographic feature height and width. See *G05* and *Trossman et al.* [2013] for additional detail.

The above version of the *G05* scheme assumes that all of the momentum stress, $\vec{\tau}$, is deposited in the bottom $H_{WD} = 500$ meters, as in *Trossman et al.* [2013, 2015], but the *G05* scheme allows for a depth- and V/N-dependent vertical deposition of momentum. The wave drag, $\tau \approx kV^3/N(\partial\eta/dz)^2$, in the hydrostatic non-rotating approximation for isopycnal displacement η, is independent of height unless the wave breaks. *G05* argues that the *Eliassen and Palm* [1961] theorem allows us to associate a particular topographic feature with a value of V that is independent of the depth until that part of the propagating (i.e., unblocked) component of the flow breaks. Meanwhile, the propagating unbroken component depends upon the amplitude of V. All depth-dependence of the wave drag is in the saturation threshold of the flow, U_c. It is also assumed that the horizontal scales of the flow do not change as a result of wave breaking, that there is no horizontal clipping, and that the disturbance cannot gain energy from the surrounding environment or radiate again from breaking regions. Pseudomomentum is deposited into layers where the propagating component of the wave drag tensor decreases with height. The propagating part of the base flux is

$$D_p(z) = a_0\rho_r \frac{(2\gamma-\epsilon)U(z)^{\gamma-\epsilon}}{U_{max}^{2\gamma-\epsilon} - U_{min}^{2\gamma-\epsilon}}(F_b + F_{ub}) \tag{A5}$$

where the broken ("b") and unbroken ("ub") parts of the field are

$$F_b = \left(\frac{U_{max}^{\gamma-\epsilon-\beta} - [u_c(0)]^{\gamma-\epsilon-\beta}}{\gamma-\epsilon-\beta} u_c(0)^\beta + \frac{[u_c(0)]^{\gamma-\epsilon} - [u_c(z)]^{\gamma-\epsilon}}{\gamma-\epsilon}\right) u_c^2 \tag{A6}$$

$$F_{ub} = \frac{[u_c(z)]^{2+\gamma-\epsilon} - U_{min}^{2+\gamma-\epsilon}}{2+\gamma-\epsilon}$$

for $U(z) = \tilde{h}\sqrt{(\rho/\rho_r)V^3/(NL_r)}$, $[u_c(z)] = min[U_{max}, max\{U_{min}, u_c\}]$, and $u_c = min_{z' \leq z}[U_c(z')]$. For the base flux calculation, V and N are taken to be averaged over the bottom 500 meters. In principle, the lee waves should be launched from the top of the deep mixed layer, V should be taken as the average velocity over the deep mixed layer, and N should be taken as the buoyancy frequency at the top of the deep mixed layer. However, the deep mixed layer is smaller than the topographic variation and it is likely that the deep mixed layer was not captured by the range of depths sampled by the profilers. Thus, we ignore the deep mixed layer for our calculations. The resulting propagating drag is clipped in the vertical so that it never increases as a function of height above the bottom. However, due to velocities that generally increase closer to the surface, the resulting dissipation can increase as a function of height above the bottom. Finally, a reference level for the non-propagating drag is found by calculating the level, z_0, at which $\int_{z_b}^{z_0} dz' N/(dU(z')/dz') = \pi$, where z_b is the seafloor depth.

References

Aguilar, D., B. Sutherland, 2006: Internal wave generation from rough topography. *Phys. Fluids*, **18**(6), 066603, doi:10.1063/1.2214538.

Arbic, B. K., S. T. Garner, R. W. Hallberg, H. L. Simmons, 2004: The accuracy of surface elevations in forward global barotropic and baroclinic tide models. *Deep-Sea Research II*, **51**, 3069–3101; doi:10.1016/j.dsr2.2004.09.014

Arbic, B. K., A. J. Wallcraft, E. J. Metzger, 2010: Concurrent simulation of the eddying general circulation and tides in a global ocean model. *Ocean Modelling*, **32**, 175–187.

Arbic, B. K., K. L. Polzin, R. B. Scott, J. G. Richman, J. F. Shriver, 2013: On eddy viscosity, energy cascades, and the horizontal resolution of gridded satellite altimeter products. *J. Phys. Oceanogr.*, **43**, 283–300.

Baines, P. G., 1995: Topographic effects in stratified flows. *Cambridge University Press*, Cambridge.

Bell Jr., T. H., 1975: Topographically generated internal waves in the open ocean. *J. Geophys. Res.*, **80**(3), 320–327.

Bretherton, F. P., 1969: Momentum transport by gravity waves. *Q. J. R. Meteorol. Soc., Ser. A*, **302**, 529–554.

Bühler, O., M. E. McIntyre, 2005: Wave capture and wave-vortex duality. *J. Fluid Mech.*, **534**, 67–95.

Eckermann, S. D., J. Lindeman, D. Broutman, J. Ma, Z. Boybeyi, 2010: Momentum fluxes of gravity waves generated by variable Froude number flow over three-dimensional obstacles. *J. Atmos. Sci.*, **67**, 2260–2278.

Eliassen, A., E. Palm, 1961: On the transfer of energy in stationary mountain waves. *Geofys. Publ.*, **22**, 1–23.

Garner, S. T., 2005: A topographic drag closure built on an analytical base flux. *J. Atmos. Sci.*, **62**, 2302–2315.

Goff, J. A., T. H. Jordan, 1988: Stochastic Modeling of Seafloor Morphology Inversion of Sea Beam Data for Second-Order Statistics, *J. Geophys. Res.*, **93**(B11), 13,589–13,608.

Goff, J. A., 2010: Global prediction of abyssal hill root-mean-square heights from small-scale altimetric gravity variability. *J. Geophys. Res.*, **115**, B12104; doi:10.1029/2010JB007867.

Goff, J. A., B. K. Arbic, 2010: Global prediction of abyssal hill roughness statistics for use in ocean models from digital maps of paleo-spreading rate, paleo-ridge orientation, and sediment thickness. *Ocean Modelling*, **32**, 36–43.

Jayne, S. R., L. C. St. Laurent, 2001: Parameterizing tidal dissipation over rough topography. *Geophys. Res. Lett.*, **28**(5), 811–814.

Lott, F., M. J. Miller, 1997: A new subgrid-scale orographic drag parametrization: its formulation and testing. *Q. J. R. Meteorol. Soc.*, **123**, 101–127.

Marshall, D. P., A. C. Naveira-Garabato, 2008: A conjecture on the role of bottom-enhanced diapycnal mixing in the parameterization of geostrophic eddies. *J. Phys. Oceanogr.*, **38**, 1607–1613.

McComas, C. H., F. P. Bretherton, 1977: Resonant interactions of oceanic internal waves. *J. Geophys. Res.*, **83**, 1397–1412.

Melet, A., R. Hallberg, S. Legg, and M. Nikurashin, 2014: Sensitivity of the ocean state to lee wave-driven mixing. *J. Phys. Oceanogr.*, **44**, 900–921.

Melet, A., R. Hallberg, A. Adcroft, M. Nikurashin, S. Legg, 2015: Energy flux into internal lee waves: sensitivity to future climate changes using linear theory and a climate model. *J. Clim.*, **28**, 2365–2384.

Naveira-Garabato, A. C., K. L. Polzin, B. A. King, K. J. Heywood, M. Visbeck, 2004: Widespread intense turbulent mixing in the Southern Ocean. *Science*, **303**, 210–213.

Naveira-Garabato, A. C., 2009: RRS *James Cook* Cruise 29, 01 Nov–22 Dec 2008. SOFine cruise report: Southern Ocean Finestructure. National Oceanography Centre Southampton Cruise Rep. 35, 216 pp.

Naveira-Garabato, A. C., A. J. G. Nurser, R. B. Scott, J. A. Goff, 2013: The impact of small-scale topography on the dynamical balance of the ocean. *J. Phys. Oceanogr.*, **43**, 647–668.

Nikurashin, M., R. Ferrari, 2010a: Radiation and dissipation of internal waves generated by geostrophic motions impinging on small-scale topography: Theory. *J. Phys. Oceanogr.*, **40**, 1055–1074.

Nikurashin, M., R. Ferrari, 2010b: Radiation and dissipation of internal waves generated by geostrophic motions impinging on small-scale topography: Application to the Southern Ocean. *J. Phys. Oceanogr.*, **40**, 2025–2042.

Nikurashin, M., S. Legg, 2011: A mechanism for local dissipation of internal tides generated at rough topography. *J. Phys. Oceanogr.*, **41**, 378–395.

Nikurashin, M., R. Ferrari, 2011: Global energy conversion rate from geostrophic flows into internal lee waves in the deep ocean. *Geophys. Res. Lett.*, **38**, L08610.

Nikurashin, M., R. Ferrari, 2013: Overturning circulation driven by breaking internal waves in the deep ocean. *Geophys. Res. Lett.*, **40**.

Nikurashin, M., R. Ferrari, N. Grisouard, K. Polzin, 2014: The impact of

finite amplitude bottom topography on internal wave generation in the Southern Ocean. *J. Phys. Oceanogr.*, **44**, 2938–2950.

Nycander, J., 2005: Generation of internal waves in the deep ocean by tides. *J. Geophys. Res.-Oceans*, **110**, C10028.

Polzin, K. L., 2008: Mesoscale eddy-internal wave coupling. Part I: Symmetry, wave capture, and results from the Mid-Ocean Dynamics Experiment. *J. Phys. Oceanogr.*, **38**, 2556–2574.

Polzin, K. L., 2010: Mesoscale eddy-internal wave coupling. Part II: Energetics and results from PolyMode. *J. Phys. Oceanogr.*, **40**, 789–801.

Polzin, K. L., A. C. Naveira Garabato, E. P. Abrahamsen, L. Jullion, M. P. Meredith, 2014: Boundary mixing in Orkney Passage outflow. *J. Geophys. Res.-Oceans*, **119**, 8627–8645, doi:10.1002/2014JC010099.

Scinocca, J. F., N. A. McFarlane, 2000: The parameterization of drag induced by stratified flow over anisotropic orography. *Quart. J. Roy. Meteor. Soc.*, **126**, 2353–2393.

Scott, R. B., B. K. Arbic, E. P. Chassignet, A. C. Coward, M. Maltrud, W. J. Merryfield, A. Srinivasan, A. Varghese, 2010: Total kinetic energy in four global eddying ocean circulation models and over 5000 current meter records. *Ocean Modelling*, **32**, 157–169.

Scott, R. B., J. A. Goff, A. C. Naveira-Garabato, A. J. G. Nurser, 2011: Global rate and spectral characteristics of internal gravity wave generation by geostrophic flow over topography. *J. Geophys. Res.*, **116**, C09029.

Shaw, T. A., T. G. Shepherd, 2007: Angular momentum conservation and gravity wave drag parameterization: implications for climate models. *J. Atmos. Sci.*, **64**, 190–203.

Shaw, T. A., M. Sigmond, T. G. Shepherd, J. F. Scinocca, 2009: Sensitivity of simulated climate to conservation of momentum in gravity wave drag parameterization. *J. Clim.*, **22**, 2726–2742.

Sheen, K. L., J. A. Brearley, A. C. Naveira-Garabato, D. A. Smeed, S. Waterman, J. R. Ledwell, M. P. Meredith, L. St. Laurent, A. M. Thurnherr, J. M. Toole, A. J. Watson, 2013: Rates and mechanisms of turbulent dissipation and mixing in the Southern Ocean: Results from the Diapycnal and Isopycnal Mixing Experiment in the Southern Ocean (DIMES). *J. Geophys. Res.-Oceans*, **118**, 1–19.

Smith, W. H. F., D. T. Sandwell, 1997: Global sea floor topography from satellite altimetry and ship depth soundings. *Science*, **277**, 1956–1962.

St. Laurent, L. C., Toole, J. M., Schmitt, R. W., 2001: Buoyancy forcing by turbulence above rough topography in the abyssal Brazil Basin. *J. Phys. Oceanogr.*, **31**, 3476–3495.

St. Laurent, L. C., H. L. Simmons, S. R. Jayne, 2002. Estimating tidally driven mixing in the deep ocean. *Geophys. Res. Lett.*, **29**, 2106.

Stern, W. F., R. T. Pierrehumbert, 1988: The impact of an orographic gravity wave drag parameterization on extended range predictions with a GCM. Preprints of the Eight Conference on Numerical Weather Prediction, American Meteorological Society, Baltimore, 745-750.

Sun. H., E. Kunze, 1999a: Internal wave-wave interactions. Part I: The role of internal wave vertical divergence. *J. Phys. Oceanogr.*, **29**, 2886–2904.

Sun, H., E. Kunze, 1999b: Internal wave-wave interactions. Part II: Spectral energy transfer and turbulence production. *J. Phys. Oceanogr.*, **29**, 2905–2919.

Trossman, D. S., B. K. Arbic, S. T. Garner, J. A. Goff, S. R. Jayne, E. J. Metzger, A. J. Wallcraft, 2013: Impact of parameterized lee wave drag on the energy budget of an eddying global ocean model. *Ocean Modelling*, **72**, 119–142.

Trossman, D. S., B. K. Arbic, J. Richman, S. T. Garner, S. R. Jayne, A. J. Wallcraft, 2015: Impact of topographic internal lee wave drag on an eddying global ocean model. *Ocean Mod-*

elling; doi:10.1016/j.ocemod.2015.10.013

Waterhouse, A. F., J. A. MacKinnon, J. D. Nash, M. H. Alford, E. Kunze, H. L. Simmons, K. L. Polzin, L. C. St. Laurent, O. M. Sun, R. Pinkel, L. D. Talley, C. B. Whalen, T. N. Huussen, G. S. Carter, I. Fer, S. Waterman, A. C. Naveira-Garabato, T. B. Sanford, C. M. Lee, 2014: Global Patterns of Diapycnal Mixing from Measurements of the Turbulent Dissipation Rate. *J. Phys. Oceanogr.*, **44**, 1854–1872.

Waterman, S., A. C. Naveira Garabato, K. L. Polzin, 2013: Internal waves and turbulence in the Antarctic Circumpolar Current. *J. Phys. Oceanogr.*, **43**, 259–282.

Waterman, S., K. L. Polzin, A. C. Naveira Garabato, K. L. Sheen, A. Forryan, 2014: Suppression of Internal Wave Breaking in the Antarctic Circumpolar Current near Topography. *J. Phys. Oceanogr.*, **44**, 1466–1492.

Webster, S., A. R. Brown, D. R. Cameron, C. P. Jones, 2003: Improvements to the representation of orography in the Met Office Unified Model. *Quart. J. Roy. Meteor. Soc.*, **129**, 1989–2010.

Wright, C. J., R. B. Scott, P. Ailliot, D. Furnival, 2014: Lee wave generation rates in the deep ocean. *Geophys. Res. Lett.*, **41**; doi:10.1002/2013GL059087.

Table 1. Corresponding to the scatterplots (Figs. 3 and 4) and four comparisons of closure predictions with estimates of the near-bottom energy dissipation rate from microstructure observations ("Obs"), we list here the spatially averaged energy conversion or dissipation rates and the average percent differences ($D = (E_{diff} - E_{ref})/E_{ref}$) either between two different predictions from lee wave closures or between a closure prediction and Obs. The percent difference is based on the difference between a prediction from one closure, E_{diff}, and a reference prediction from either one other closure or the observed value, E_{ref} [in W m^{-2}]. A standard error, $\sigma_{E_{ref}}$, of the mean E_{ref} and a 95% confidence interval, $D_{E,CI}$, for the difference $E_{diff} - E_{ref}$ are listed. The saturation correction factor is used each time the *B75* theory is utilized, except in the first two entries of this table. The shorthand notation utilized in this table is described at the beginning of section 4. Arithmetic averages are used. (Our results are not qualitatively altered when geometric averages are utilized.) The number of data points, N_{data}, utilized in the comparisons with Obs is different from that utilized in the other comparisons due to the smaller number of station locations where both finestructure and microstructure data are available. The number of data points utilized in the closure prediction comparisons also varies due to the varying number of station locations where internal waves have wavenumbers that lie within the radiative range, (8).

Differenced prediction	Reference prediction	E_{ref} ($\sigma_{E_{ref}}$)	D ($D_{E,CI}$)	N_{data}
B75 aniso V_{const} N_{const}	*B75* approx iso V_{const} N_{const}	6.8×10^{-3} (5.9×10^{-4})	-82% (-2.4×10^{-3}, -5.1×10^{-3})	66
B75 aniso V_{const} N_{const}	*B75* iso V_{const} N_{const}	4.7×10^{-4} (2.6×10^{-5})	160% (1.1×10^{-3}, 4.2×10^{-4})	66
G05 aniso V_{const} N_{const} $Z = H_{ref}$	*B75* aniso V_{const} N_{const}	8.5×10^{-4} (6.3×10^{-5})	-76% (-3.5×10^{-4}, 3.0×10^{-4})	67
G05 aniso V_{const} N_{const} $Z = H_{rms}$	*B75* aniso V_{const} N_{const}	8.5×10^{-4} (6.3×10^{-5})	-5.3% (-3.4×10^{-4}, 2.5×10^{-4})	67
G05 aniso V N $Z = H_{ref}$	*B75* aniso V N	1.1×10^{-3} (1.0×10^{-2})	-95% (-3.1×10^{-2}, 8.9×10^{-3})	62
G05 aniso V N $Z = H_{rms}$	*B75* aniso V N	1.1×10^{-3} (1.0×10^{-2})	27% (-2.1×10^{-2}, 2.8×10^{-2})	62
B75 approx iso V N	Obs	9.7×10^{-4} (3.0×10^{-4})	1030% (3.5×10^{-4}, 1.3×10^{-2})	61
B75 iso V N	Obs	9.7×10^{-4} (3.0×10^{-4})	-65% (-1.9×10^{-3}, -7.2×10^{-5})	61
B75 aniso V N	Obs	9.7×10^{-4} (3.0×10^{-4})	16% (-7.7×10^{-3}, 3.4×10^{-2})	61
G05 aniso V N $Z = H_{rms}$	Obs	9.7×10^{-4} (3.0×10^{-4})	480% (8.9×10^{-4}, 3.2×10^{-2})	61
G05 aniso V N $Z = H_{ref}$	Obs	9.7×10^{-4} (3.1×10^{-4})	9.7% (-9.0×10^{-4}, 4.4×10^{-3})	61

Table 2. Corresponding to the scatterplots shown in Figs. 3 and 4a-d and four comparisons of closure predictions with estimates of the near-bottom energy dissipation rate from microstructure observations ("Obs"), listed are the Pearson correlation coefficients, ρ_{corr} (and their 95% confidence intervals), between the abscissa and ordinate pairs. The saturation correction factor is used each time the *B75* theory is utilized, except in the first two entries of this table.

Ordinate	Abscissa	ρ_{corr} (95% confidence interval)
B75 aniso V_{const} N_{const}	*B75* approx iso V_{const} N_{const}	-0.63 (-0.77,-0.44)
B75 aniso V_{const} N_{const}	*B75* iso V_{const} N_{const}	0.98 (0.97,0.99)
G05 aniso V_{const} N_{const} $Z = H_{ref}$	*B75* aniso V_{const} N_{const}	0.53 (0.31,0.69)
G05 aniso V_{const} N_{const} $Z = H_{rms}$	*B75* aniso V_{const} N_{const}	1.0 (1.0,1.0)
G05 aniso V N $Z = H_{ref}$	*B75* aniso V N	0.75 (0.66,0.82)
G05 aniso V N $Z = H_{rms}$	*B75* aniso V N	0.92 (0.87,0.95)
Obs	*B75* approx iso V N	-0.14 (-0.43,0.18)
Obs	*B75* iso V N	0.17 (-0.17,0.47)
Obs	*B75* aniso V N	0.10 (-0.22,0.40)
Obs	*G05* aniso V N $Z = H_{rms}$	0.26 (-0.055,0.53)
Obs	*G05* aniso V N $Z = H_{ref}$	0.13 (-0.19,0.43)

Table 3. For each of the closure predictions compared with observations in Tables 1-2, listed are the heights above the seafloor that the average vertical profiles of the observed turbulent kinetic energy dissipation rates would need to be integrated to in order to achieve closest agreement with the closure predictions.

closure	height integrated from seafloor
B75 approx iso V N	$>$ 4000 m
B75 iso V N	$<$ 100 m
B75 aniso V N	860 m
G05 aniso V N $Z = H_{rms}$	$>$ 4000 m
G05 aniso V N $Z = H_{ref}$	720 m

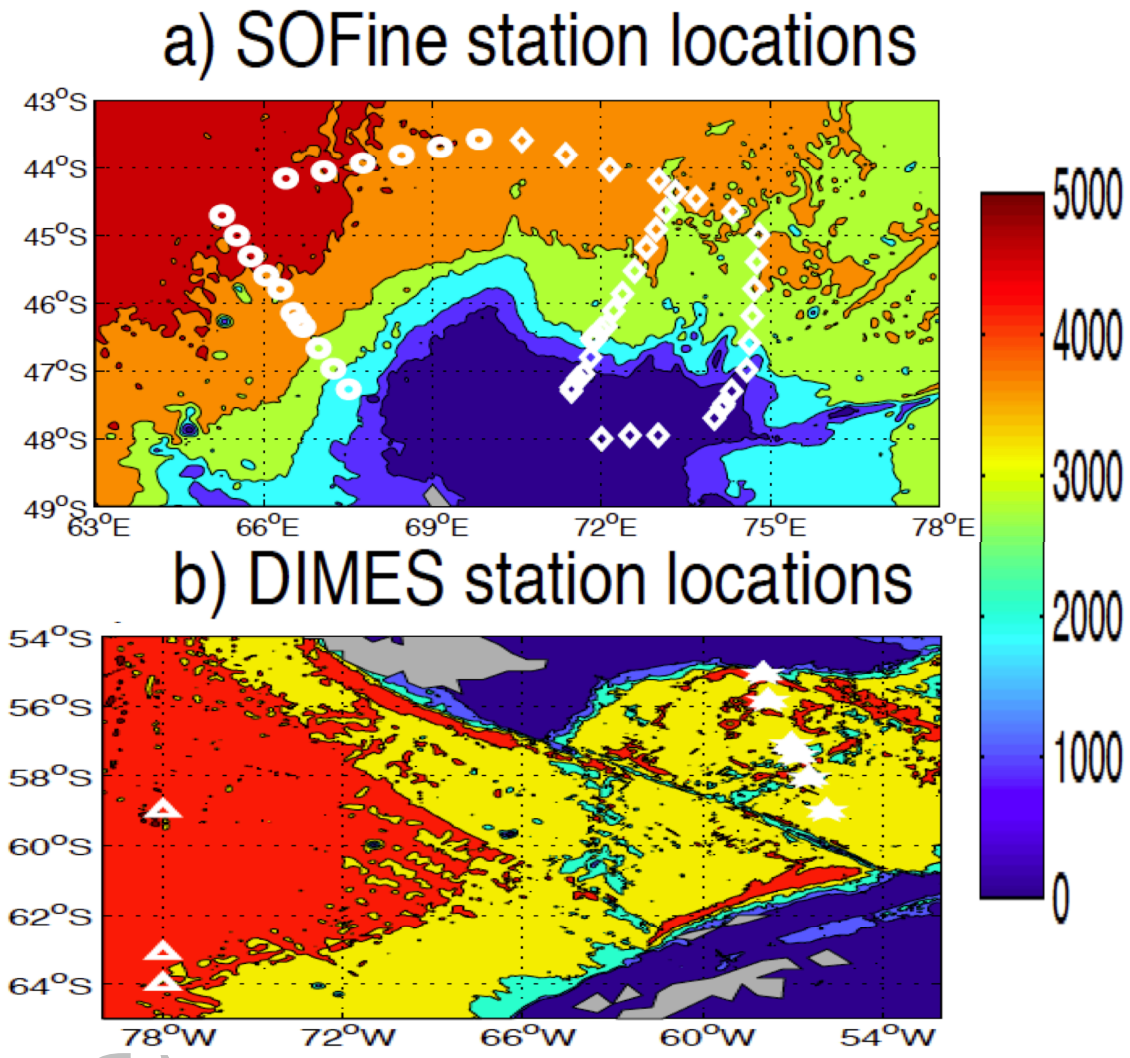

Figure 1. The station locations from (a) the SOFine data - western (white circles) and eastern (white diamonds), (b) the T1 transect of the DIMES data (white triangles), and (b) the T4 transect of the DIMES data (white stars). The seafloor depth (in meters; *Smith and Sandwell*, 1997) is also shown with its scale given by the colorbar.

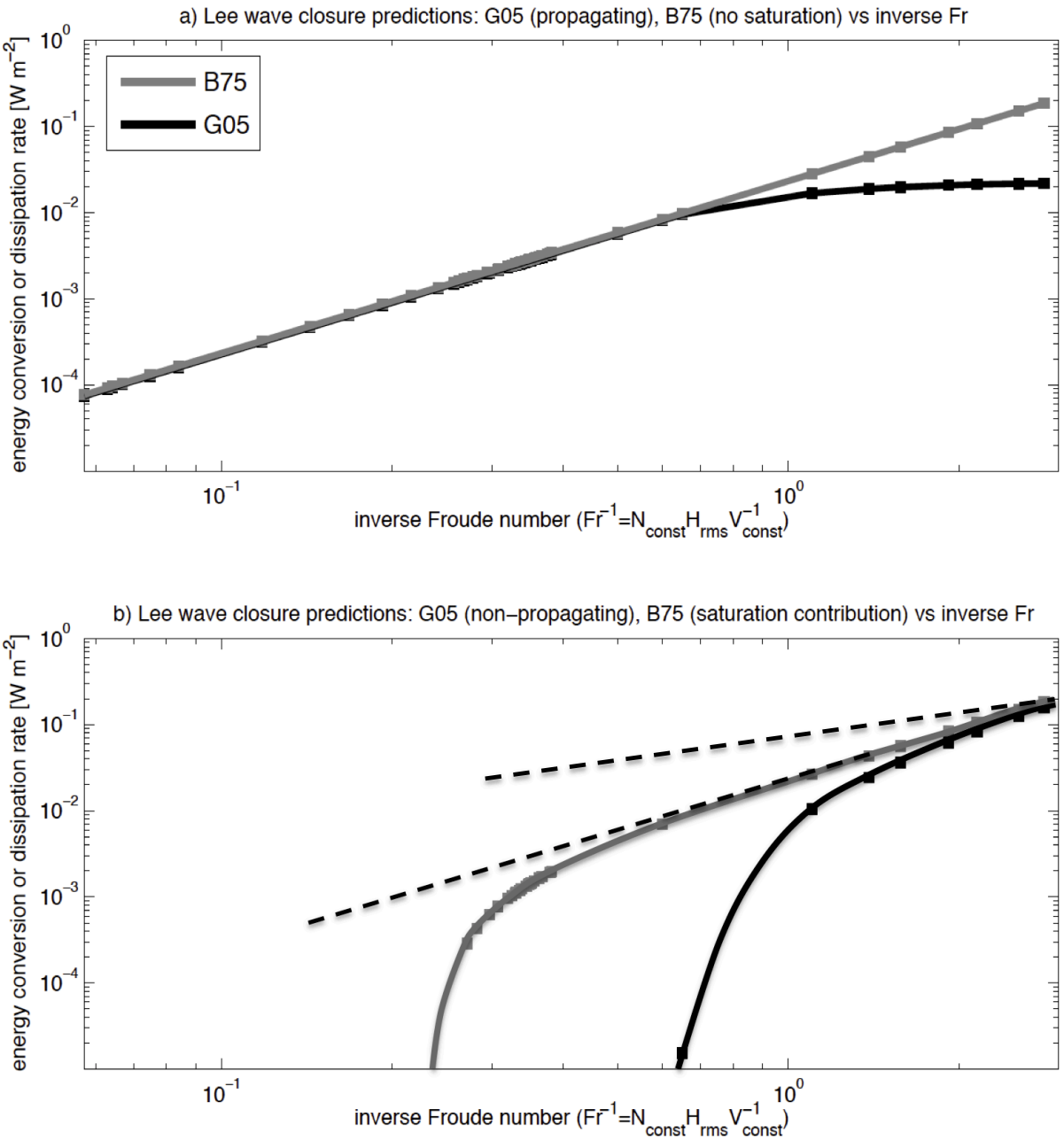

Figure 2. (a) The energy conversion rates from *B75* V_{const} N_{const} versus the propagating energy dissipation rates from *G05* V_{const} N_{const}. (b) The energy conversion rate differences from *B75* V_{const} N_{const} without minus with the saturation correction factor versus the non-propagating energy dissipation rates from *G05* V_{const} N_{const}. We use approximated isotropic underlying topography with (5), and we allow only H_{rms} to vary from station to station (i.e., k_0 and μ are constant, equal to their station-averaged values). The solid grey curves go through the predictions from the *B75* theory. The solid black curves go through the predictions from the *G05* scheme. The dashed black lines indicate slopes of 2 and 1.

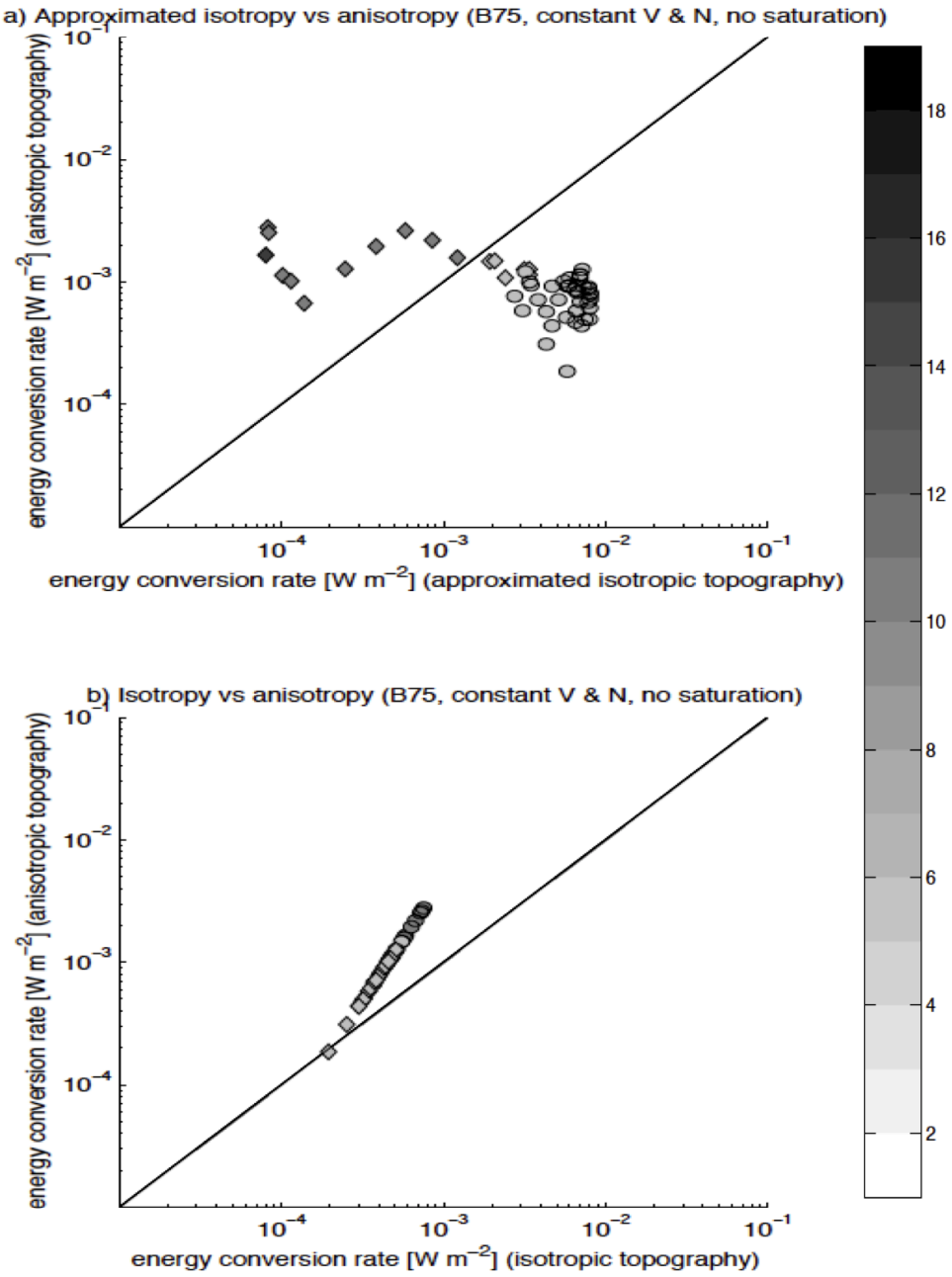

Figure 3. Energy conversion rates from *B75* aniso V_{const} N_{const} versus those from (a) *B75* approx iso V_{const} N_{const} and (b) *B75* iso V_{const} N_{const}. The one-to-one correspondence line is the solid black line. Darker (lighter) shadings correspond to larger (smaller) Froude numbers (see colorbar). The circles (diamonds) are derived from the western (eastern) SOFine near-bottom velocities and buoyancy frequencies, and the triangles (stars) are derived from the T1 (T4) transect of the DIMES near-bottom velocities and buoyancy frequencies.

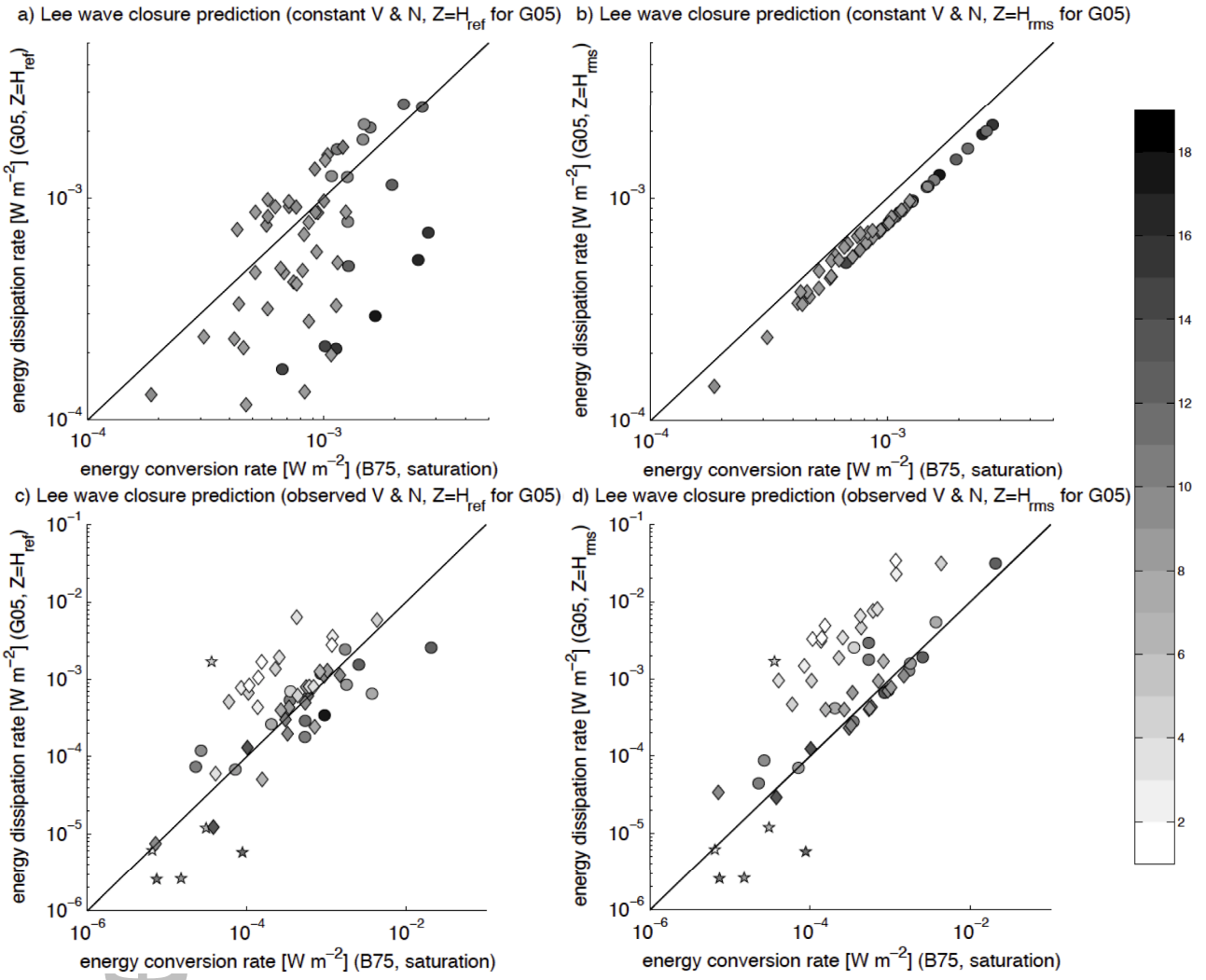

Figure 4. Energy dissipation rate versus energy conversion rate predictions from (a) from *G05* aniso V_{const} N_{const} ($Z = H_{ref}$) versus *B75* aniso V_{const} N_{const}, (b) from *G05* aniso V_{const} N_{const} ($Z = H_{rms}$) versus *B75* aniso V_{const} N_{const}, (c) from *G05* aniso V N ($Z = H_{ref}$) versus *B75* aniso V N, and (d) from *G05* aniso V N ($Z = H_{rms}$) versus *B75* aniso V N. The saturation correction factor is included for all predictions using the *B75* theory. The one-to-one correspondence line is the solid black line. Darker (lighter) shadings correspond to larger (smaller) Froude numbers. See the colorbar for the range of Froude numbers shown here. Note that the range on each axis is different in panels a-b from panels c-d. The circles (diamonds) are derived from the western (eastern) SOFine near-bottom velocities and buoyancy frequencies, and the triangles (stars) are derived from the T1 (T4) transect of the DIMES near-bottom velocities and buoyancy frequencies.

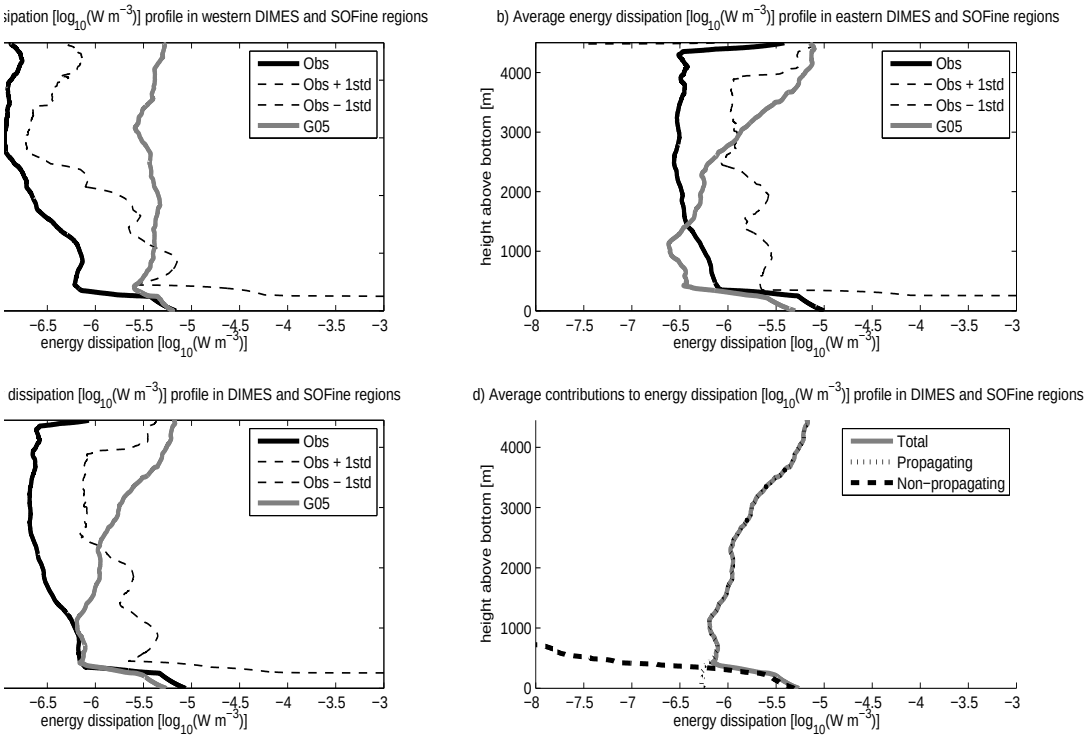

Figure 5. Shown are the geometrically averaged vertical profiles of the energy dissipation rates inferred from the microstructure observations (black) and the *G05* scheme (grey) over the western (panel a) and eastern (panel b) and all (panel c) DIMES and SOFine station locations. For each panel in this figure, in contrast to earlier figures, the *G05* scheme is allowed to deposit the momentum flux over a large portion of the water column. The western station locations include the circles and triangles in Fig. 1 and eastern station locations include the diamonds and stars in Fig. 1. The dashed lines shown indicate $\pm$ one standard deviation over all station locations at each height above the deepest profiler measurement, or "bottom". Also shown are the profiles of the predicted propagating (dotted black), non-propagating (dashed black), and total (solid grey) dissipation, geometrically averaged over all of the DIMES and SOFine station locations (panel d).

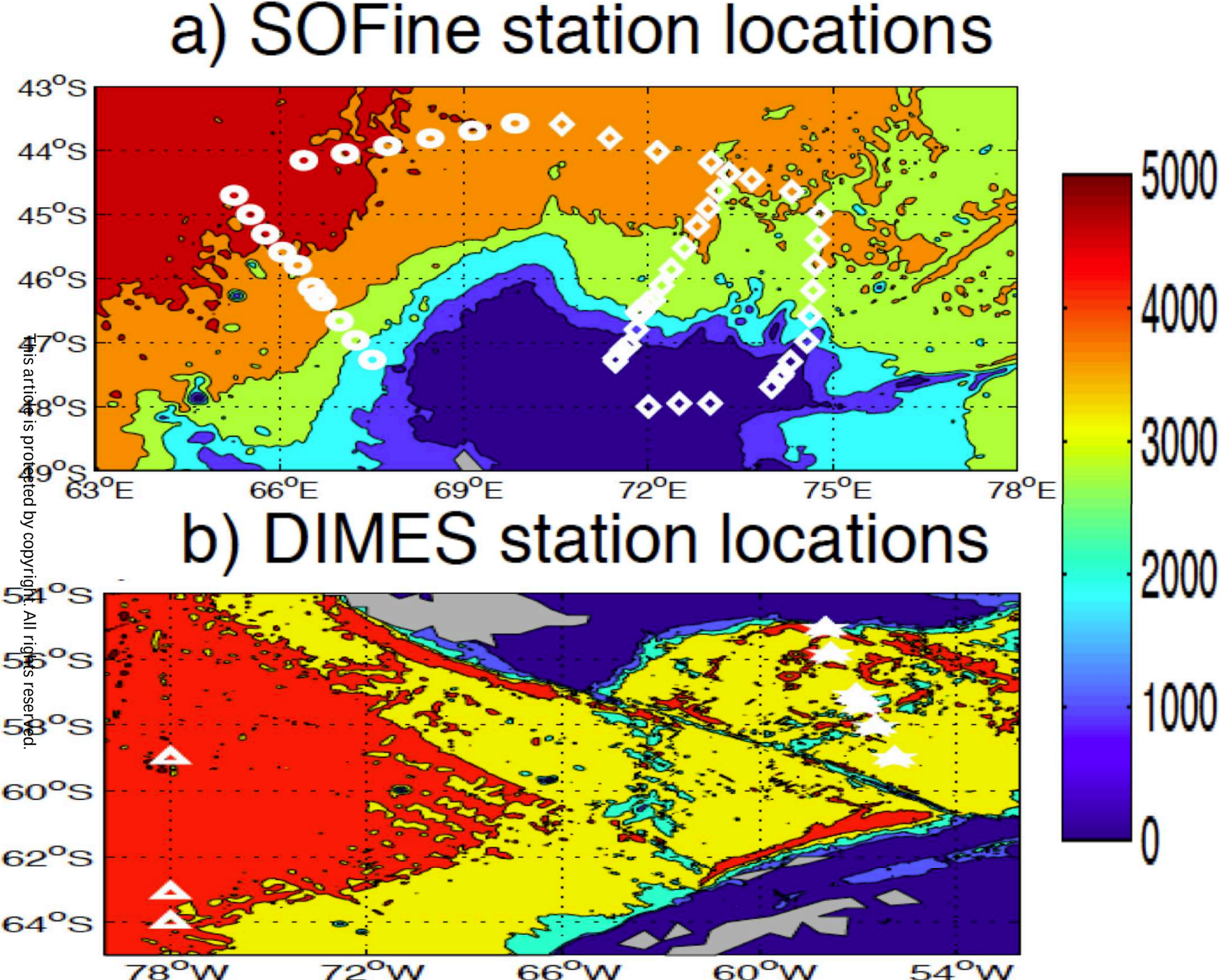

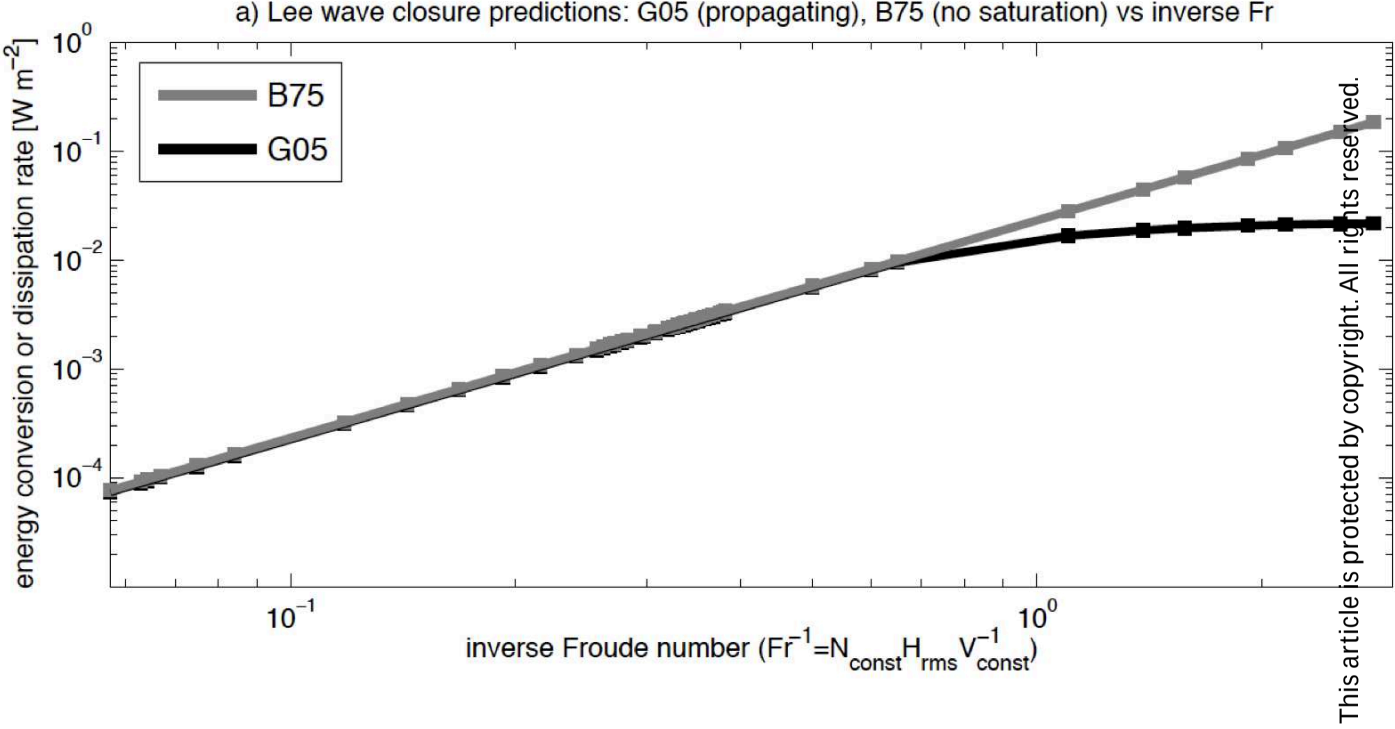

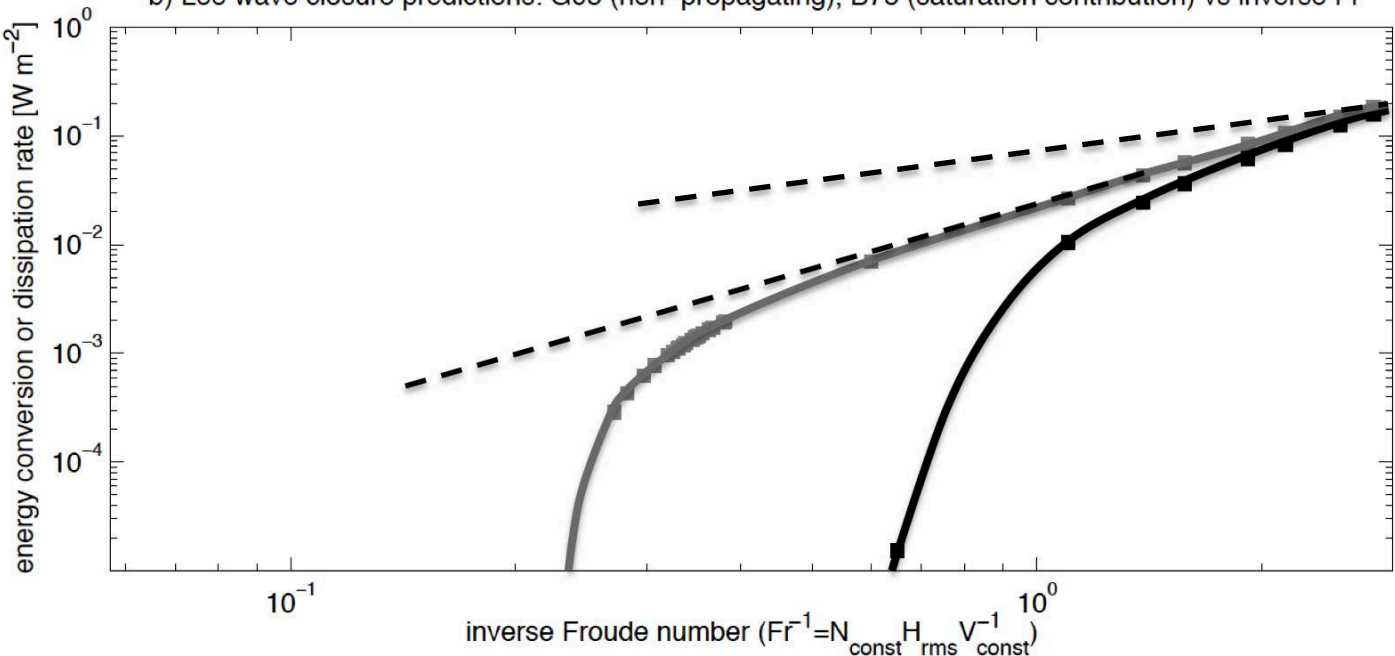

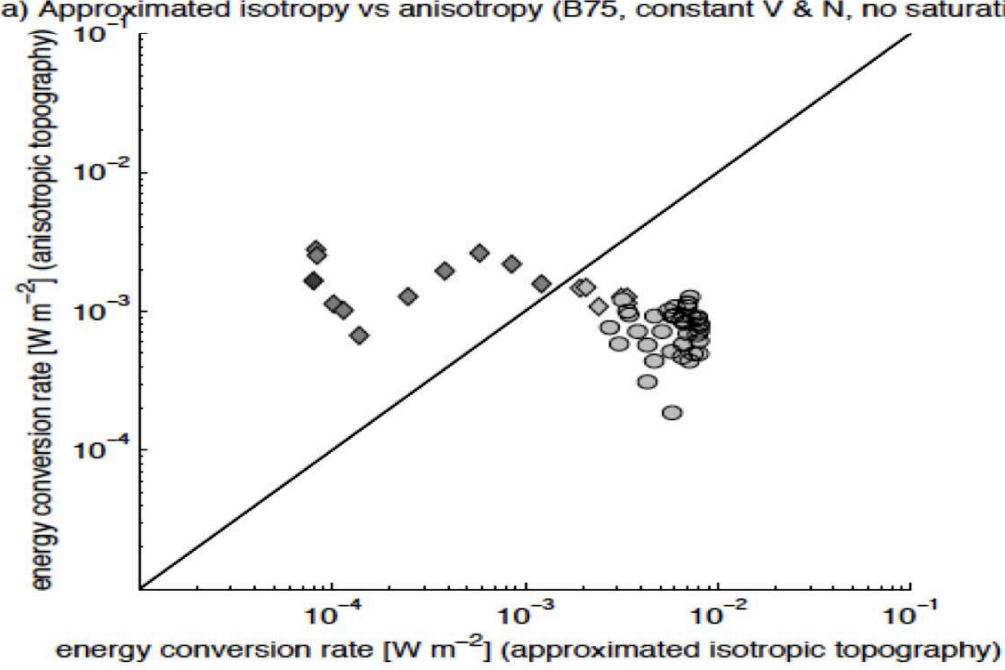
a) Approximated isotropy vs anisotropy (B75, constant V & N, no saturation)
energy conversion rate [W m^{-2}] (anisotropic topography)
energy conversion rate [W m^{-2}] (approximated isotropic topography)
10^{-1}
10^{-2}
10^{-3}
10^{-4}

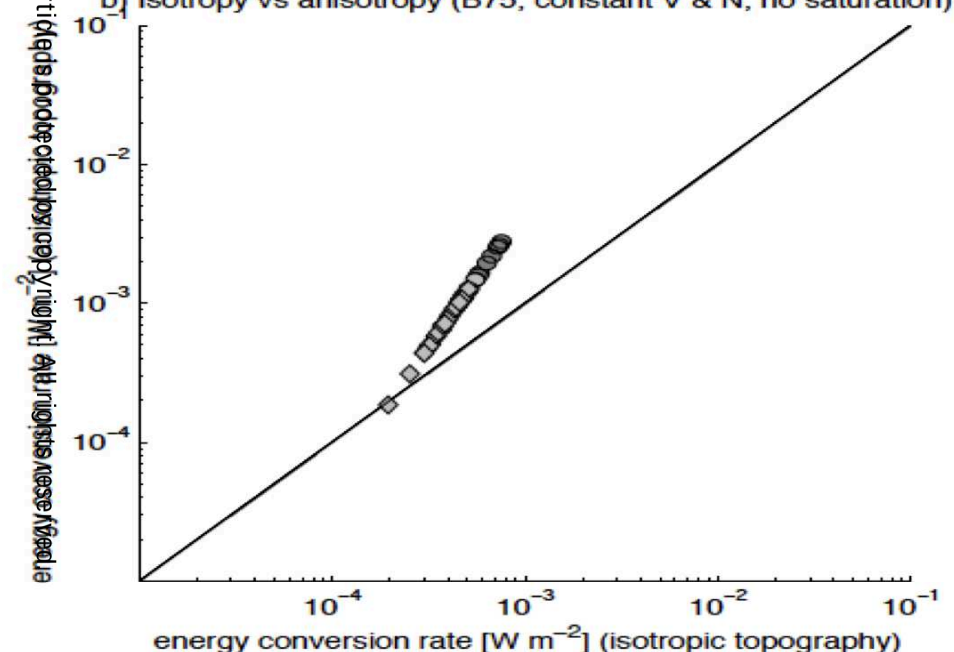
b) Isotropy vs anisotropy (B75, constant V & N, no saturation)
energy conversion rate [W m^{-2}] (isotropic topography)
10^{-1}
10^{-2}
10^{-3}
10^{-4}


18
16
14
12
10
8
6
4
2

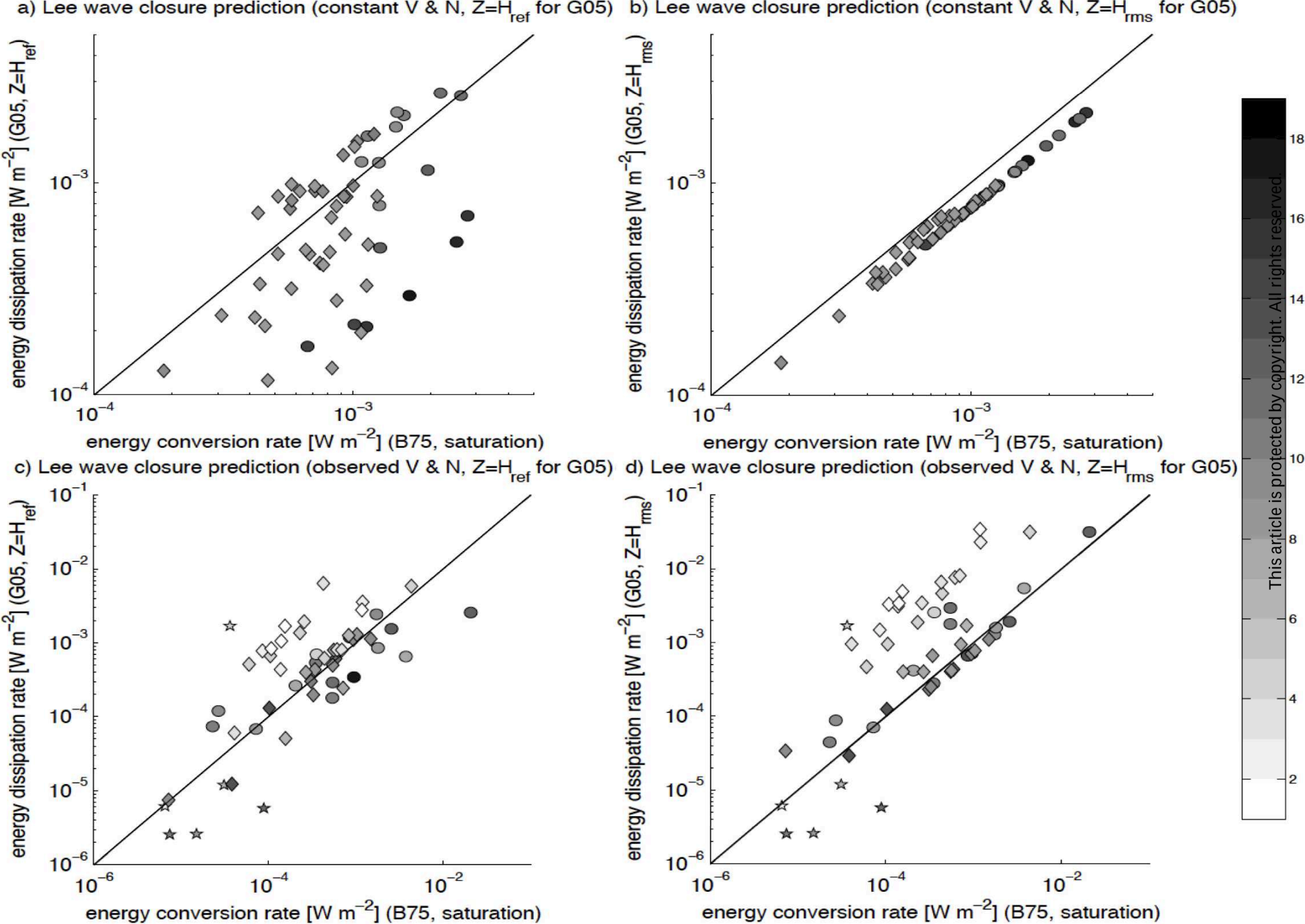
a) Lee wave closure prediction (constant V & N, Z=H_ref for G05)
b) Lee wave closure prediction (constant V & N, Z=H_rms for G05)
c) Lee wave closure prediction (observed V & N, Z=H_ref for G05)
d) Lee wave closure prediction (observed V & N, Z=H_rms for G05)
energy dissipation rate [W m^-2] (G05, Z=H_ref)
energy dissipation rate [W m^-2] (G05, Z=H_rms)
energy conversion rate [W m^-2] (B75, saturation)
This article is protected by copyright. All rights reserved.

a) Average energy dissipation [$\log_{10}$(W m^{-3})] profile in western DIMES and SOFine regions

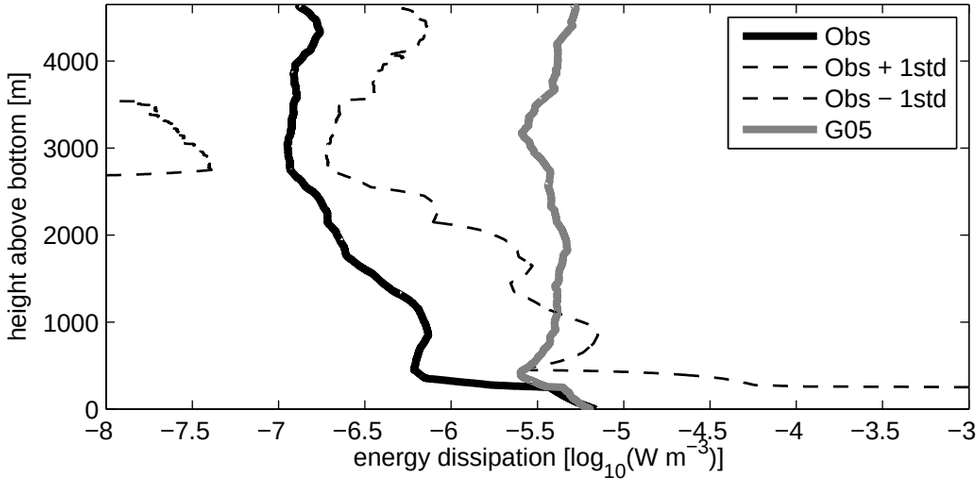

b) Average energy dissipation [$\log_{10}$(W m^{-3})] profile in eastern DIMES and SOFine regions

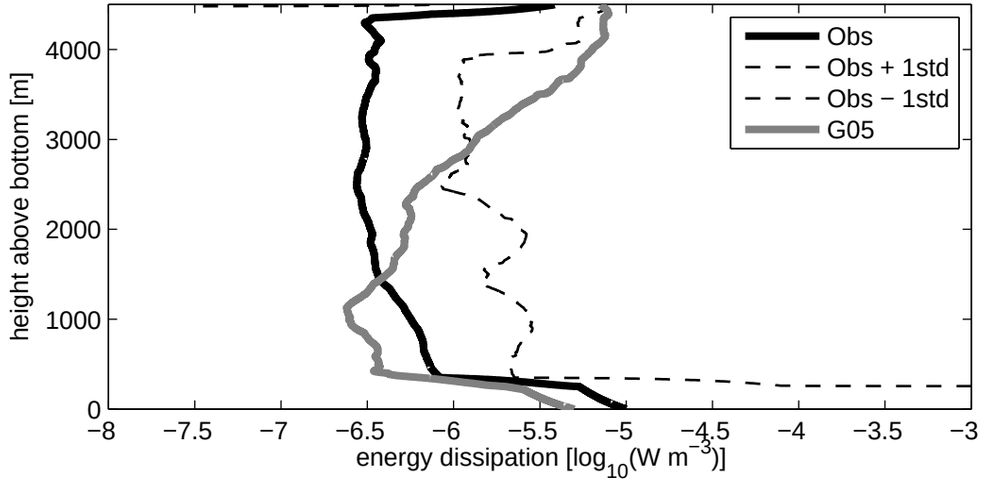

c) Average energy dissipation [$\log_{10}$(W m^{-3})] profile in DIMES and SOFine regions

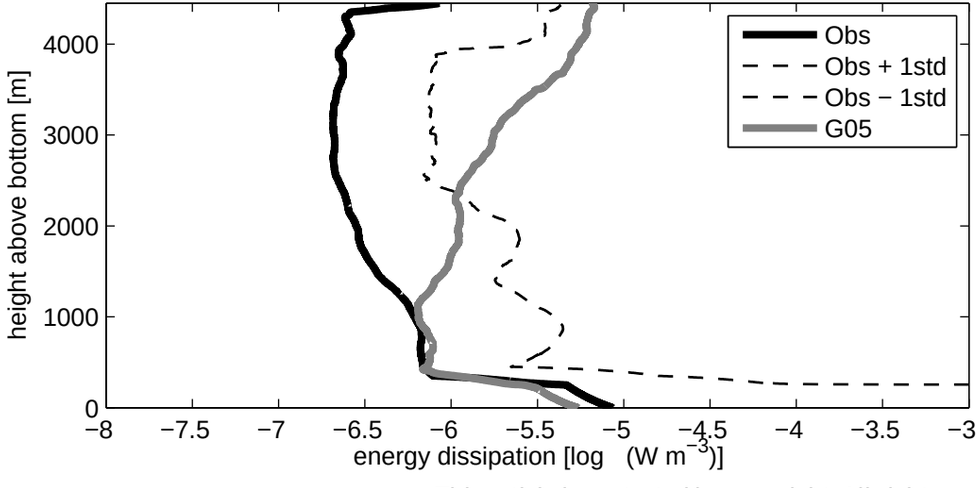

d) Average contributions to energy dissipation [$\log_{10}$(W m^{-3})] profile in DIMES and SOFine regions